Integrating Cloud Processes in the Community Atmosphere Model, Version 5

SUNGSU PARK

National Center for Atmospheric Research, Boulder, Colorado

CHRISTOPHER S. BRETHERTON

University of Washington, Seattle, Washington

PHILIP J. RASCH

Pacific Northwest National Laboratory, Richland, Washington

ABSTRACT

This paper provides a description of the integrated representation for the cloud processes in the Community Atmosphere Model, version 5 (CAM5). CAM5 cloud parameterizations add the following unique characteristics to previous versions: 1) a cloud macrophysical structure with horizontally nonoverlapped deep cumulus, shallow cumulus, and stratus in each grid layer, where each of which has its own cloud fraction, and mass and number concentrations for cloud liquid droplets and ice crystals; 2) stratus–radiation–turbulence interactions that allow CAM5 to simulate marine stratocumulus solely from grid-mean relative humidity without relying on a stability-based empirical formula; 3) prognostic treatment of the number concentrations of stratus liquid droplets and ice crystals, with activated aerosols and detrained in-cumulus condensates as the main sources and with evaporation, sedimentation, and precipitation of stratus condensate as the main sinks; and 4) radiatively active cumulus and snow. By imposing consistency between diagnosed stratus fraction and prognosed stratus condensate, unrealistically empty or highly dense stratus is avoided in CAM5. Because of the activation of the prognostic aerosols and the parameterizations of the radiation and stratiform precipitation production as a function of the cloud droplet size, CAM5 simulates various aerosol indirect effects as well as the direct effects: that is, aerosols affect both the radiation budget and the hydrological cycle.

Detailed analysis of various simulations indicates that CAM5 improves upon CAM3/CAM4 in global performance as well as in physical formulation. However, several problems are also identified in CAM5, which can be attributed to deficient regional tuning, inconsistency between various physics parameterizations, and incomplete treatment of physics. Efforts are continuing to further improve CAM5.

1. Introduction

Clouds cool the earth–atmosphere system by reflecting incoming shortwave (SW) radiation and warm it by absorbing outgoing longwave (LW) radiation from the surface. Satellite observations reveal that the net radiative effect of clouds on the earth–atmosphere system is a cooling of 20–24 W m^{-2} in the global annual average (SW cooling of 47–54 W m^{-2}; LW warming of 26–30 W m^{-2}), about 6 times larger than the radiative forcing

associated with doubled CO_2 (Ramanathan et al. 1989; Loeb et al. 2009). To the first order, SW radiation reflected by clouds and LW radiation absorbed by clouds are proportional to the cloud fraction and in-cloud optical thickness that is (inversely) proportional to the in-cloud condensate amount (cloud droplet radius). Clouds are central to the global hydrological cycle. In the global annual mean, the sink of atmospheric moisture by precipitation should balance the upward moisture flux from the earth's surface. If evaporation is neglected, the global-mean precipitation rate at the surface is the product of the cloud fraction and in-cloud production rate of precipitation that is proportional to the in-cloud condensate amount and cloud droplet radius. Clouds also play an important role in the vertical transport of

Corresponding author address: Sungsu Park, Climate and Global Dynamics Division, National Center for Atmospheric Research, P.O. Box 3000, Boulder, CO 80307.
E-mail: sungsup@ucar.edu

heat, moisture, momentum, and aerosols. The formation and dissipation of clouds that regulate the global radiation budget and the hydrological cycle is controlled by this vertical transport, which in turn is strongly influenced by the radiative and hydrological properties of clouds. This indicates the existence of complex feedback processes among cloud dynamics, radiation, and precipitation. To correctly assess future climate change, we need a good representation of global cloud properties (cloud fraction, in-cloud condensate, and cloud droplet radius), the factors that control the variations of cloud properties, and the feedback between cloud properties and controlling factors.

We have worked on developing a new version of the Community Atmosphere Model (CAM5) that provides the community with a state-of-the-art GCM that can simulate cloud–aerosol–climate interactions in a physically reasonable way. Compared to the previous versions, CAM5 contains many new physics parameterizations, including the following: 1) a moist turbulence scheme (Bretherton and Park 2009) that performs subgrid vertical transport by both dry and moist turbulent eddies throughout the whole atmosphere, replacing CAM3's dry PBL scheme (Holtslag and Boville 1993); 2) a shallow convection scheme (Park and Bretherton 2009) that performs subgrid vertical transport by a convective inhibition (CIN)-based, ensemble-mean updraft plume with a penetrative entrainment closure at the cumulus top, replacing CAM3's shallow convection scheme (Hack 1994); 3) a deep convection scheme that has a dilute convective available potential energy (CAPE)-based closure (Neale et al. 2008), with vertical transport of horizontal momentum (Richter and Rasch 2008); 4) a double-moment stratiform microphysics scheme (Morrison and Gettelman 2008), replacing CAM3's single-moment stratiform microphysics scheme (Rasch and Kristjansson 1998); 5) a modal aerosol model that computes the mass and number conversion rates between various prognostic aerosol species and performs droplet activation and ice nucleation (Liu et al. 2012), replacing CAM3's bulk aerosol model; and 6) an improved radiation scheme (Iacono et al. 2008). Altogether, CAM5 is designed to improve simulation of the global radiation budget and hydrological cycle; the subgrid vertical transport of heat, moisture, momentum, and aerosols; and complex feedbacks among cloud dynamics, radiation, and precipitation processes. This is achieved by improving the subgrid representation of cumulus and stratus and the interactions between different physics parameterizations associated with the clouds and aerosols (see Fig. 1).

Compared with the previous versions, the cloud parameterizations in CAM5 are more consistent and physically based. Several key aspects of CAM5 cloud parameterizations are as follows:

- a consistent cloud macrophysical formulation;
- stratus–radiation–turbulence interactions;
- prognostic treatment of stratus droplet number and aerosol species; and
- radiatively active cumulus and snow.

This paper describes the CAM5 cloud macrophysics scheme, which provides a framework for the horizontal and vertical distribution of clouds (see Fig. 2). Section 2 provides a detailed description of the cloud macrophysical structure in CAM5, including how CAM5 computes cloud fraction, in-cloud condensate amount, and the droplet number concentration for deep and shallow cumulus and stratus clouds, and a description of how to impose consistency between the diagnosed stratus fraction and prognosed in-stratus condensate in appendix A. Section 3 contrasts CAM5-simulated cloud properties compared with CAM3/CAM4 and observations, with discussion on the source of improvements from CAM3/CAM4 and the source of discrepancies against observations at the process level. A summary and conclusion is provided in section 4.

2. Cloud structures in CAM5

Cloud is a volume containing hydrometeors suspended in the atmosphere. CAM5 has two types of clouds: cumulus and stratus. Cumulus consists of deep and shallow cumulus, while stratus consists of liquid and ice stratus. In contrast to CAM3/CAM4, CAM5 does not have a stability-based stratiform cloud but has a relative humidity (RH)-based stratiform cloud that is referred to as stratus throughout this paper. In the case that the horizontal grid size $G \equiv \Delta x \Delta y$ (where Δx and Δy are the zonal and meridional width of the model grid) is comparable to or larger than the size of the compensating subsidence induced by a typical convective updraft observed in nature, CAM5-simulated cumulus and stratus are analogous to the observed cumulus and stratus, respectively. If G becomes small, however, such analogy is broken, and special attention is necessary in comparing the simulated and observed cloud components and associated precipitation rates (Park 2014a,b).

CAM5 defines the following five quantities for each cloud type in each layer: cloud fraction (A), in-cloud liquid water content ($\hat{q}_l$), in-cloud ice water content ($\hat{q}_i$), in-cloud liquid droplet radius ($\hat{r}_l$), and in-cloud ice crystal radius ($\hat{r}_i$). At times, the model recognizes that cloud may be internally heterogeneous and defines in-cloud distributions of q_l, q_i, r_l, and r_i. This section provides a summary of how CAM5 simulates 1) the
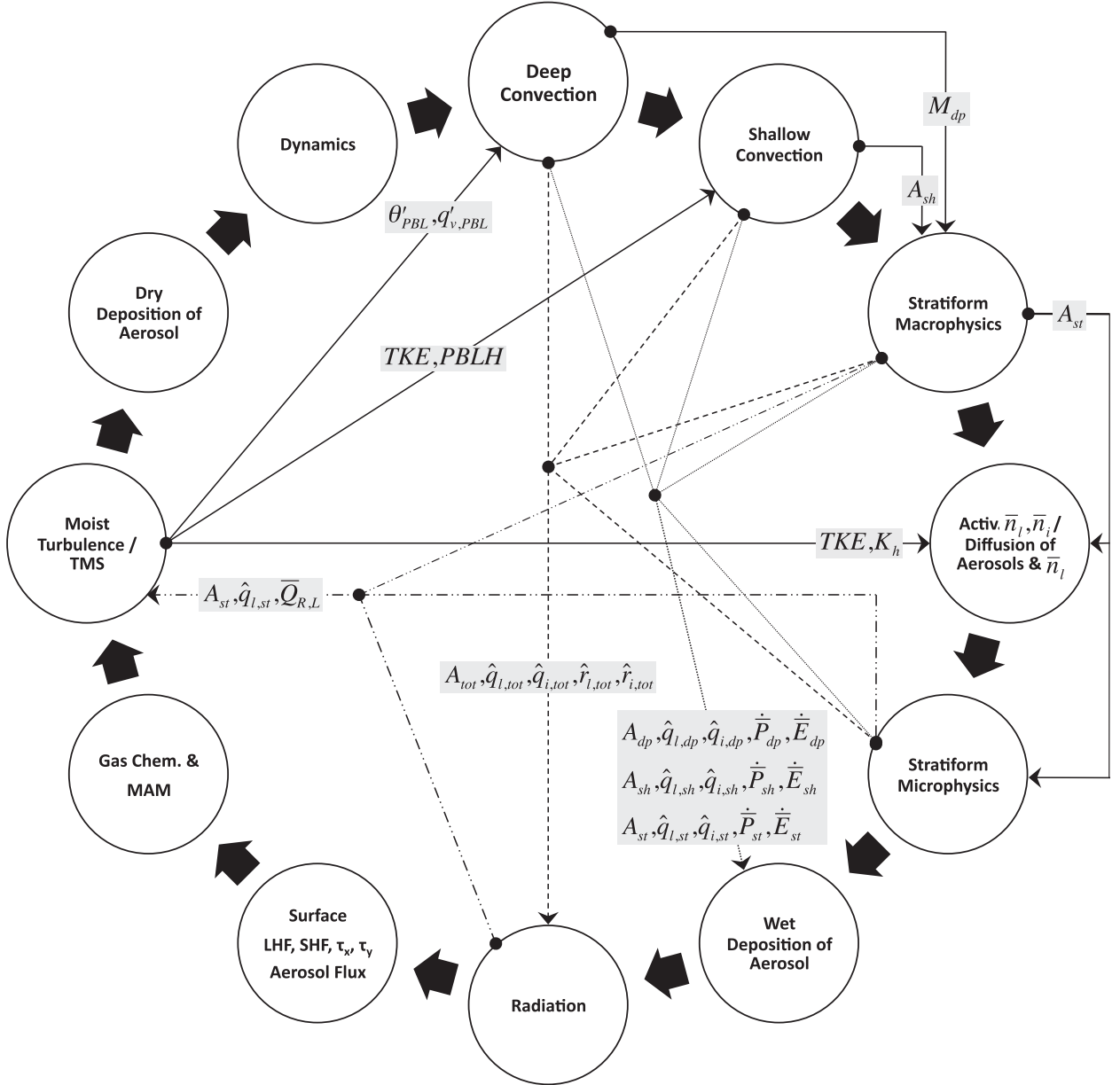
FIG. 1. A diagram illustrating interactions among various physics and dynamic processes in CAM5. Thick arrows denote a sequence of process splitting at each time step with a flow of normal grid-mean state variables of $\phi = T, q_v, q_l, q_i, u, v, \zeta_i,$ and ζ_c, where ζ_i and ζ_c are the mass and number concentrations of 15 interstitial (i.e., outside of cloud liquid droplets and ice crystals) and stratus-borne aerosol species, respectively. Thin arrows denote the flows of additional variables [turbulent kinetic energy (TKE), PBL top height (PBLH); eddy diffusivity for heat and moisture K_h; $A, q_l, q_i, n_l, n_i, r_l,$ and r_i are cloud fraction and condensate mass, number concentration, and radius of cloud liquid droplets and ice crystals; subscripts dp, sh, st, and tot denote deep cumulus, shallow cumulus, stratus, and total clouds; the overbar and hat denote grid-mean and in-cloud average, respectively; $Q_{R,L}$ is LW radiative cooling rate; P and E are precipitation production and evaporation; M is convective mass flux; and θ'_{PBL} and $q'_{v,PBL}$ are convective excess of temperature and moisture within PBL; surface latent flux (LHF) and sensible flux (SHF); τ_x and τ_y are surface wind stresses; and modal aerosol model (MAM); and implicit turbulent mountain stress (TMS) parameterized as a function of subgrid variation of topography and grid-mean static stability at the lowest model interface above the surface]. CAM5 prints most cloud diagnostics at the beginning of the radiation scheme.

aforementioned five cloud properties ($A, q_l, q_i, r_l,$ and r_i) for deep and shallow cumulus and stratus and 2) the horizontal and vertical overlapping structures between different cloud types. In each of the following

subsections, the parameterizations of cloud fraction, cloud condensate amount, and cloud droplet radius are described. CAM5 prognoses grid-mean droplet number concentrations ($\overline{n}_l$ and $\overline{n}_i$), which are used to compute $\hat{r}_l$

$$A_{clr} = 1 - (A_{dp} + A_{sh} + A_{st})$$

$$\tilde{q}_{v,clr}, \tilde{\xi}_{clr}$$
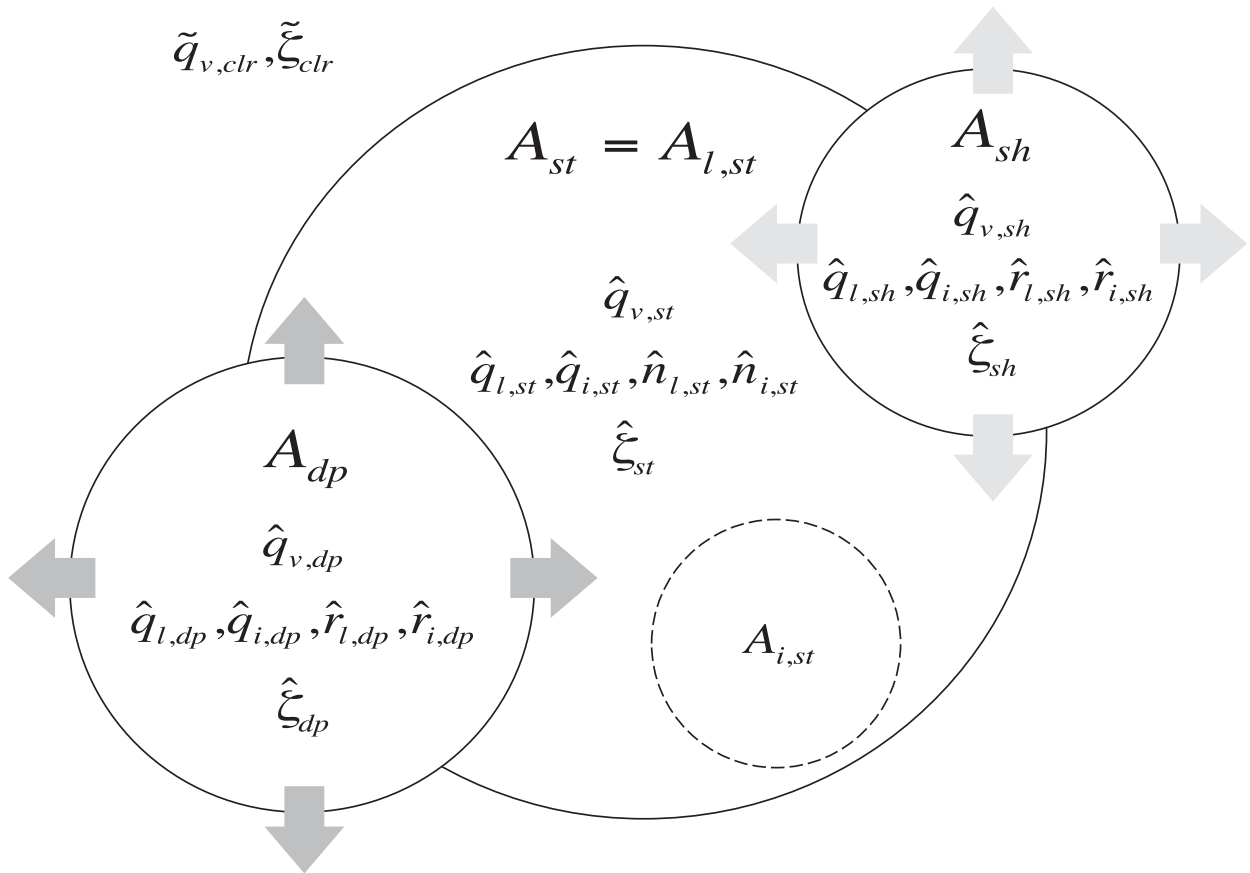
FIG. 2. A diagram illustrating cloud macrophysical structures in CAM5 that have nonoverlapped deep cumulus, shallow cumulus, and stratus in each layer: each of which has its own cloud fraction, mass, and number concentration of cloud droplets. A single stratus fraction (A_{st}) is obtained by assuming maximum overlap between liquid stratus ($A_{l,st}$) and ice stratus ($A_{i,st}$), and then in-stratus LWC/IWC are uniformly distributed over A_{st}. In this figure, $A_{i,st}$ is located within $A_{l,st}$, so that $A_{st} = \max(A_{l,st}, A_{i,st}) = A_{l,st}$. CAM5 assumes that any stratus in the vertical path of convective updraft (either shallow or deep) is displaced by the convective updraft, resulting in the horizontal nonoverlap between stratus and cumulus, as shown above. The tilde denotes the average over the clear portion. Thick arrows denote convective condensate detrained into the environment randomly without preferred spots. See the caption of Fig. 1 for the meaning of each variable.

and $\hat{r}_i$ by assuming a certain drop size distribution. Figure 2 provides a schematic diagram of the cloudy and cloud-free (i.e., clear) components in each layer. Throughout this paper, we will use the following conventions: 1) subscripts dp (deep cumulus), sh (shallow cumulus), cu (cumulus, which is the sum of deep and shallow cumulus), st (stratus), and tot (total cloud, which is the sum of cumulus and stratus); 2) subscripts l (liquid), i (ice), and c (condensate, which is the sum of liquid and ice); 3) overbars (e.g., $\bar{\zeta}$) for quantities with a grid-mean value excluding a cumulus portion; and 4) hats (e.g., $\hat{\zeta}$) for in-cloud value.

a. Cumulus

CAM5 has separate deep and shallow convection schemes, where each of which computes a cloud fraction

A, and in-cloud condensate amount $\hat{q}_l$ and $\hat{q}_i$ of a single ensemble-mean convective updraft plume from the base to the top of the convective updraft. Because of the zero storage assumption of quasi-steady convective plumes, internal thermodynamic properties of cumulus are not advected by the grid-mean advection scheme (i.e., the in-cumulus content is not a part of the grid-mean content) but the radiative effect of cumulus is explicitly treated. Since cumulus microphysics is a single moment, only diagnosing the vertical profile of condensate mass, CAM5 needs to specify the cumulus droplet radius and its distribution in order to compute the radiative effects of in-cumulus and detrained convective condensate and the microphysical effects (e.g., the production rate of stratiform precipitation) of detrained convective condensate in the stratus. Unlike for stratus, CAM5

computes a single-phase (no separate liquid and ice phases) cumulus fraction for both deep and shallow cumulus. From the viewpoint of subgrid turbulence dynamics, stratus is the saturated portion of local symmetric turbulent eddies, while cumulus is the saturated portion of nonlocal asymmetric turbulent updraft eddies (Park 2014a).

1) DEEP CUMULUS

With a set of thermodynamic properties of source air estimated from the grid-mean values at the level of maximum moist static energy (z_*) and surface fluxes, a deep convective updraft plume rises from z_* with a specified lateral entrainment rate if the dilute CAPE [a vertical integral of updraft buoyancy from z_* to the level of neutral buoyancy (LNB)] computed by assuming a constant entrainment rate of $1 \times 10^{-3}\,\mathrm{m}^{-1}$ is larger than $70\,\mathrm{J\,kg}^{-1}$. CAM5 computes the deep cumulus fraction a_{dp} using the following empirical formula:

$$a_{\mathrm{dp}} = 0.1 \times \ln(1 + 500 M_{\mathrm{dp}}),$$
$$a_{\mathrm{dp}} = \max[0, \min(a_{\mathrm{dp}}, 0.6)], \quad (1)$$

where M_{dp} is net updraft mass flux of a deep convective plume (in units of $\mathrm{kg\,m}^{-2}\,\mathrm{s}^{-1}$) and the two coefficients 0.1 and 500 are tunable parameters.

Deep cumulus below the lifting condensation level (LCL) is empty (i.e., in-cumulus condensate $\hat{q}_{c,\mathrm{dp}} \equiv \hat{q}_{l,\mathrm{dp}} + \hat{q}_{i,\mathrm{dp}} = 0$ but $A_{\mathrm{dp}} > 0$). Some of $\hat{q}_{c,\mathrm{dp}}$ generated above the LCL is precipitated out at a rate of $\overline{P}_{\mathrm{dp}} = c_0 \hat{q}_{c,\mathrm{dp}} M_{\mathrm{dp}}$, where c_0 is a fractional autoconversion efficiency of cumulus condensate into convective precipitation specified differently over ocean ($c_{0,\mathrm{ocn}} = 4.5 \times 10^{-2}\,\mathrm{m}^{-1}$) and land ($c_{0,\mathrm{lnd}} = 5.9 \times 10^{-3}\,\mathrm{m}^{-1}$) to crudely account for higher aerosol concentration and smaller droplet radius over land than over the ocean. The ice fraction ($f_{\mathrm{dp},i}$) of $\hat{q}_{c,\mathrm{dp}}$ for convective dynamics within the deep convection scheme is set to 0, except for the dilute CAPE computation, which assumes $f_{\mathrm{dp},i} = 0$ (1) if in-cumulus temperature is larger (smaller) than 273.15 K. For radiative treatment of in-cumulus condensate, we assume $f_{\mathrm{dp},i} = f_{\mathrm{st},i}$ but $f_{\mathrm{dp},i} = 0$ if no stratus exists in the same layer. For detrained convective condensate, we assume $f_{\mathrm{dp},i} = 0$ (1) if $\overline{T} > 268.15\,\mathrm{K}\,(< 238.15\,\mathrm{K})$ with a ramping function between the two temperature ranges.

For radiative treatment, CAM5 assumes in-cumulus condensate has the same droplet radius and size distribution parameters as in-stratus condensate in the same layer. If stratus does not exist in the same layer, CAM5 specifies an effective diameter of $50\,\mu\mathrm{m}$ for cumulus ice crystals and shape and slope parameters of a gamma

distribution of 5.3 and $(5.3 + 1)/25\,\mu\mathrm{m}^{-1}$ for cumulus liquid droplets, respectively. For detrained cumulus condensate, the effective volume radius is set to 8 (25) $\mu\mathrm{m}$ for liquid droplets (ice crystals) at all heights.

2) SHALLOW CUMULUS

A shallow convective updraft plume rises from the PBL top with lateral entrainment and detrainment rates inversely proportional to the geometric height. Since it is a dynamic plume model, the CAM5 shallow convection scheme computes the vertical velocity ($\hat{w}_{\mathrm{sh}}$) as well as the mass flux (M_{sh}) of a single ensemble-mean convective updraft plume. The shallow cumulus fraction a_{sh} is computed using M_{sh} and $\hat{w}_{\mathrm{sh}}$ from the LCL (or the PBL top if the LCL is within the PBL) to the cumulus top where $\hat{w}_{\mathrm{sh}} = 0$,

$$a_{\mathrm{sh}} = 2\left(\frac{M_{\mathrm{sh}}}{\rho \hat{w}_{\mathrm{sh}}}\right), \quad a_{\mathrm{sh}} = \max[0, \min(a_{\mathrm{sh}}, 0.2)], \quad (2)$$

where ρ is air density. Similar to the CAPE closure used in the deep convection scheme, the CIN closure used in the shallow convection scheme is designed to simulate only the positively buoyant convective updrafts growing above the LFC. We multiply by a factor of 2 in Eq. (2) to account for negatively buoyant as well as positively buoyant saturated convective updrafts.

In contrast to deep cumulus, there is no empty shallow cumulus since a_{sh} is computed from the LCL. If $\hat{q}_{c,\mathrm{sh}} > 0.7\,\mathrm{g\,kg}^{-1}$, the excessive in-cumulus condensate ($\hat{q}_{c,\mathrm{ex}} = \hat{q}_{c,\mathrm{sh}} - 0.7$) is assumed to precipitate out. The ice fraction ($f_{\mathrm{sh},i}$) of $\hat{q}_{c,\mathrm{sh}}$ for convective dynamics within the shallow convection scheme is assumed 0 (1) if in-cumulus temperature is higher (lower) than 268 (248) K with a ramping function between the limits. For radiative treatment of in-cumulus and detrained cumulus condensates, we set $f_{\mathrm{sh},i} = f_{\mathrm{dp},i}$.

The droplet size distributions of in-cloud and detrained shallow cumulus condensates are specified in the same way as deep cumulus, except for the use of 10 (50) $\mu\mathrm{m}$ as the effective volume radius of detrained shallow cumulus liquid droplets (ice crystals).

b. Stratus

Both CAM3 and CAM4 diagnosed a single-phase stratus fraction (a_{st}) as a quadratic function of grid-mean RH $\overline{u}$. However, the CAM5 stratus macrophysics scheme diagnoses separate liquid and ice stratus fractions ($a_{l,\mathrm{st}}$, $a_{i,\mathrm{st}}$) using grid-mean RH over water ($\overline{u}_l \equiv \overline{q}_v / \overline{q}_{s,w}$, where $\overline{q}_v$ is the grid-mean water vapor specific humidity and $\overline{q}_{s,w}$ is the grid-mean saturation specific humidity over water) and grid-mean total ice RH over ice

$[\overline{v}_i \equiv (\overline{q}_v + \overline{q}_i)/\overline{q}_{s,i}$, where $\overline{q}_{s,i}$ is the grid-mean saturation specific humidity over ice], respectively. Except for computing $\overline{u}_l$ and $\overline{v}_i$, grid-mean temperature $\overline{T}$ is not explicitly used in diagnosing $a_{l,\text{st}}$ and $a_{i,\text{st}}$. Ideally, all subsequent physics parameterizations should be separately applied to liquid, ice, and mixed-phase stratus. However, CAM5 uniformly distributes $\overline{q}_{l,\text{st}}$ and $\overline{q}_{i,\text{st}}$ over the single a_{st}, which is computed by assuming maximum horizontal overlap between $a_{l,\text{st}}$ and $a_{i,\text{st}}$ [i.e., $a_{\text{st}} = \max(a_{l,\text{st}}, a_{i,\text{st}})$], and all subsequent physics parameterizations (e.g., aerosol activation and nucleation, stratus microphysics, wet deposition of aerosols, radiation, aerosol conversion, subgrid vertical transport by moist turbulence, and deep and shallow convection) are operating on a single a_{st}. The CAM5 stratus macrophysics scheme also computes the grid-mean net condensation rate of water vapor into liquid stratus condensate ($\overline{Q}_l$) and associated changes of $\overline{T}$. A focus on internal consistency between the diagnosed stratus fraction and prognosed stratus condensate guarantees that both liquid and ice stratus are neither empty nor dense at the end of stratus macrophysics. However, since subsequent

stratus microphysics can completely deplete all $\overline{q}_{l,\text{st}}$ and $\overline{q}_{i,\text{st}}$ into precipitation, stratus could become empty after stratus microphysics. CAM5 does not perform any additional procedure to remove empty stratus (e.g., recomputation of stratus fraction or a consistency-imposing procedure after stratiform microphysics) until it is handled by stratus macrophysics at the next time step. The following subsections provide details of how CAM5 computes cloud fraction, condensate amount, and the droplet radius of liquid and ice stratus before being supplied to the radiation scheme.

1) LIQUID STRATUS

CAM5 diagnoses $a_{l,\text{st}}$ based on the assumption that the subgrid distribution of total liquid RH v_l follows a triangular probability density function (PDF), where $v_l \equiv q_{t,l}/\overline{q}_{s,w}$: $q_{t,l}$ is the total liquid specific humidity ($= q_v + q_l$) and $\overline{q}_{s,w}$ is grid-mean saturation specific humidity over water. Then $a_{l,\text{st}}$ becomes a unique function of grid-mean RH over water, $\overline{u}_l$ (see appendix A for derivation),

$$a_{l,\text{st}} = \begin{cases} 1, & \text{if } \overline{u}_l \geq \hat{u}_l, \\ 1 - \left[\dfrac{3}{\sqrt{2}}\left(\dfrac{\hat{u}_l - \overline{u}_l}{\hat{u}_l - u_{\text{cl}}}\right)\right]^{2/3}, & \text{if } \dfrac{1}{6}(5\hat{u}_l + u_{\text{cl}}) \leq \overline{u}_l \leq \hat{u}_l, \\ 4\cos\left[\dfrac{1}{3}\left\{\arccos\left[\dfrac{3}{2\sqrt{2}}\left(\dfrac{\overline{u}_l - u_{\text{cl}}}{\hat{u}_l - u_{\text{cl}}}\right)\right] - 2\pi\right\}\right]^2, & \text{if } u_{\text{cl}} \leq \overline{u}_l \leq \dfrac{1}{6}(5\cdot\hat{u}_l + u_{\text{cl}}), \\ 0, & \text{if } \overline{u}_l \leq u_{\text{cl}}, \end{cases} \tag{3}$$

where $\hat{u}_l = 1$ is in-cloud RH over water within $a_{l,\text{st}}$, $u_{\text{cl}} = \hat{u}_l - \Delta v_l$ is a critical RH at which liquid stratus $a_{l,\text{st}}$ starts to form, and Δv_l is the half-width of the triangular distribution. The quantity $a_{l,\text{st}}$ can also be formulated as a function of $\overline{v}_l$ instead of $\overline{u}_l$ [Eq. (A2)]. In order for Eq. (3) to be applicable in any GCM grid size as a scale-adaptive parameterization, Δv_l should be internally computed rather than externally specified, by considering all sources of subgrid variability (e.g., local symmetric turbulence, detrained convective air, subgrid mesoscale organized flows, gravity waves, and surface inhomogeneity). However, CAM5 uses u_{cl} as a tuning parameter depending on geometric height and surface properties with $u_{\text{cl}} = 0.89$ in the layers below 700 hPa (low-level stratus) but $u_{\text{cl}} = 0.79$ over land if water-equivalent snow depth is less than 10^{-6} m (a crude parameterization to represent larger subgrid variability

over a rougher surface in the lower troposphere), $u_{\text{cl}} = 0.80$ in the layers above 400 hPa (high-level stratus), and a linearly interpolated u_{cl} is used between the two heights (midlevel stratus).

In principle, both $a_{l,\text{st}}$ and $\overline{Q}_l$ can be diagnosed in a consistent way from the triangular PDF. However, CAM5 uses a separate prognostic condensation scheme to compute $\overline{Q}_l$. Two sufficient and necessary assumptions used for computing $\overline{Q}_l$ in CAM5 are 1) RH over water within liquid stratus is always 1 ($\hat{u}_l = 1$) and 2) liquid stratus condensate does not exist outside of $a_{l,\text{st}}$ ($\tilde{q}_l = 0$, where the tilde denotes the region outside of $a_{l,\text{st}}$), which together will be called saturation equilibrium. Whenever any layer is perturbed from the saturation equilibrium state by external forcings (e.g., radiative cooling or grid-scale advection of water vapor or liquid water), CAM5 tries to restore the saturation

equilibrium state and $\overline{Q}_l$ is a consequence of this saturation equilibrium adjustment, as detailed in appendix A. The separate computations of diagnostic $a_{l,st}$ and prognostic $\overline{Q}_l$ can cause inconsistency between $a_{l,st}$ and $\hat{q}_{l,st}$, such as empty stratus (i.e., $a_{l,st} > 0$ but $\hat{q}_{l,st} = 0$) or dense stratus (i.e., very large $\hat{q}_{l,st}$). Imposing consistency between $a_{l,st}$ and $\hat{q}_{l,st}$ is very important in the process-splitting CAM5, since subsequent stratus microphysics, wet deposition of aerosols, radiation, and moist turbulence schemes require consistent inputs (see Fig. 1). CAM5 is carefully designed to remove inconsistencies (detailed in appendix A) by 1) computing $\overline{Q}_l$ using saturation equilibrium state variables at the end of the previous time step's stratus macrophysics, 2) computing a single $a_{l,st}$ at each time step using the updated saturation equilibrium state at the end of the current time step's stratus macrophysics, and 3) performing corrective pseudo condensation-evaporation to ensure $\hat{q}_{l,st,min} = 2 \times 10^{-4} < \hat{q}_{l,st} < \hat{q}_{l,st,max} = 3\,\mathrm{g\,kg^{-1}}$ at the end of stratus macrophysics.

Once consistent values of $a_{l,st}$ and $\hat{q}_{l,st}$ are generated by stratus macrophysics, subsequent aerosol activation and stratus microphysics schemes perform conversion processes from aerosols to cloud condensation nuclei (CCN) and from cloud condensate to precipitation as described in Liu et al. (2012) and Morrison and Gettelman (2008), respectively. The CAM5 moist turbulence and grid-scale advection schemes treat all prognostic grid-mean tracers (including water constituents, $\overline{q}_v = \overline{q}_{v,st}$, $\overline{q}_l = \overline{q}_{l,st}$, and $\overline{q}_i = \overline{q}_{i,st}$) as conservative scalars without phase changes during transport. The associated phase change of transported $\overline{q}_l$ (i.e., $\overline{Q}_l$) is handled by stratus macrophysics using saturation equilibrium constraints at the next time step. The deep convection scheme can increase $\overline{q}_{l,st}$ by detraining some in-cumulus condensate in the layers from the level of minimum grid-mean moist static energy in the middle and upper troposphere to the cumulus top. The shallow convection scheme can also change $\overline{q}_{l,st}$ by detraining some in-cumulus condensate in the layers between cumulus base and cumulus top, with additional influence by compensating subsidence.

CAM5 prognoses the number concentrations ($\overline{n}_{l,st}$, $\overline{n}_{i,st}$) as well as the mass ($\overline{q}_{l,st}$, $\overline{q}_{i,st}$) of stratus liquid droplets and ice crystals. If $\overline{Q}_l > 0$, stratus macrophysics does not change $\overline{n}_{l,st}$ (because of the assumption that condensation occurs on the existing cloud droplets); however, if $\overline{Q}_l < 0$, $\overline{n}_{l,st}$ is reduced in proportion to the decrease of $\overline{q}_{l,st}$ [i.e., $\Delta\overline{n}_{l,st} = \overline{Q}_l \Delta t (\overline{n}_{l,st}/\overline{q}_{l,st})$], which ensures $\overline{n}_{l,st} = 0$ if $\overline{q}_{l,st} = 0$ at the end of stratus macrophysics. If $\overline{Q}_l > 0$ in the initially clear layer, the updated $\overline{q}_{l,st} > 0$ while $\overline{n}_{l,st} = 0$. No adjustment is made to impose consistency for this case, since the following aerosol activation routine generates $\overline{n}_{l,st}$. Subgrid vertical transport of $\overline{n}_{l,st}$ by local symmetric turbulent eddies is performed after stratus macrophysics, in conjunction with vertical transport of aerosols and activation of transported aerosols into CCN using an explicit diffusion solver with the implicit eddy diffusivities computed from the moist turbulence scheme at the previous time step (Fig. 1). The deep convection scheme can increase $\overline{n}_{l,st}$ by detraining some in-cumulus condensate with a specified effective volume radius of $8\,\mu\mathrm{m}$. The shallow convection scheme can also change $\overline{n}_{l,st}$ by detraining some in-cumulus condensate with a specified effective volume radius of $10\,\mu\mathrm{m}$, with additional changes by compensating subsidence. The grid-scale advection scheme transports $\overline{n}_{l,st}$ in the same way as the other grid-mean water constituents and aerosol species, by treating each transported species as an independent conservative scalar, without further attempt to impose consistency among species (e.g., $\overline{q}_l$ and $\overline{n}_l$) after transport.

2) ICE STRATUS

CAM5 diagnoses the ice stratus fraction $a_{i,st}$ as a quadratic function of grid-mean total ice RH over ice, $\overline{v}_i \equiv \overline{q}_{t,i}/\overline{q}_{s,i}$, where $\overline{q}_{t,i} = \overline{q}_v + \overline{q}_i$ is the grid-mean total ice specific humidity and $\overline{q}_{s,i}$ is the grid-mean saturation specific humidity over ice,

$$a_{i,st} = \left(\frac{\overline{v}_i - u_{ci}}{\hat{u}_i - u_{ci}}\right)^2, \qquad (4)$$

where $\hat{u}_i \geq 1$ is the in-cloud RH over ice within $a_{i,st}$ and u_{ci} is the critical RH at which ice stratus starts to form. In contrast to Eq. (3), no direct association exists between Eq. (4) and the PDF of $v_i = q_{t,i}/\overline{q}_{s,i}$. Supersaturation within $a_{i,st}$ is allowed by setting $\hat{u}_i > 1$. CAM5 chooses $\hat{u}_i = 1.1$ and $u_{ci} = 0.80$, regardless of geometric height and surface properties. At the end of stratus macrophysics, CAM5 enforces $\hat{q}_{i,st,min} = 2 \times 10^{-4} < \hat{q}_{i,st} < \hat{q}_{i,st,max} = 5\,\mathrm{g\,kg^{-1}}$ by adjusting $a_{i,st}$ (instead of doing corrective pseudo deposition–sublimation). This removes empty and unrealistically dense ice stratus but violates Eq. (4) (see appendix A for details).

Rather than using saturation equilibrium constraints for ice stratus with $\hat{u}_i \geq 1$, CAM5 computes $\overline{Q}_i$ (the grid-mean net deposition rate of water vapor into ice stratus condensate) using an explicit process formula. In mixed-phase stratus, $\overline{Q}_i$ can be positive only after cloud water from preexisting stratus liquid droplets is completely transformed into ice crystals by the Bergeron–Findeisen process. The way that CAM5 prognoses $\overline{q}_i = \overline{q}_{i,st}$ in various physics and dynamics schemes is similar to that for $\overline{q}_l = \overline{q}_{l,st}$ described in the previous section.

CAM5 prognoses $\overline{n}_i = \overline{n}_{i,\text{st}}$ similar to the way that $\overline{n}_l = \overline{n}_{l,\text{st}}$ is updated (described in the previous section), except that 1) aerosol nucleation into ice crystals is invoked, instead of aerosol activation into liquid droplets; 2) specified effective ice volume radii of 25 and 50 μm are assumed for detrained cumulus ice crystals from the deep and shallow convection schemes, respectively; and 3) the implicit diffusion solver within the moist turbulence scheme is used to perform subgrid vertical transport of $\overline{n}_{i,\text{st}}$ in conjunction with conservative transport of $\overline{q}_{i,\text{st}}$.

c. Cloud overlap

Within each grid layer, CAM5 diagnoses four independent cloud fractions for deep and shallow cumulus and liquid and ice stratus ($0 \leq a_{\text{dp}} \leq 0.6$, $0 \leq a_{\text{sh}} \leq 0.2$, $0 \leq a_{l,\text{st}}$, and $a_{i,\text{st}} \leq 1$, respectively) and the associated in-cloud condensate mass and number concentration ($\hat{q}_l$, $\hat{q}_i$ and $\hat{n}_l$, $\hat{n}_i$). The performance of individual physics schemes is sensitive to how these clouds are distributed horizontally and vertically. For example, if $a_{l,\text{st}}$ and $a_{i,\text{st}}$ are maximally (minimally) overlapped in the horizontal, Bergeron–Findeisen conversion from stratus liquid droplets to ice crystals will be maximized (minimized). Convective condensate detrained into the clear (stratus) portion of the grid layer will (will not) be evaporated. Vertical profiles of grid-mean radiative flux, production and evaporation rates of convective and stratiform precipitation, and activation and wet deposition of aerosols are sensitive to the vertical overlapping structure of clouds. Given that CAM5 prognoses not only $\overline{q}_l$ and $\overline{q}_i$ but also $\overline{n}_l$ and $\overline{n}_i$ (or equivalently $\hat{r}_l$ and $\hat{r}_i$), which have direct influences on the computation of radiative flux and the production rate of stratiform precipitation, appropriate parameterizations of activation and wet deposition of aerosols become especially important for reasonable simulation of cloud–climate feedbacks in CAM5. Hence, the cloud overlap should be carefully formulated and, if possible, a single cloud overlap structure should be consistently used for all parameterizations. This section describes the horizontal and vertical overlap structure of clouds in CAM5.

1) HORIZONTAL OVERLAP

CAM5 assumes that 1) a_{dp} and a_{sh} are nonoverlapped; 2) $a_{l,\text{st}}$ and $a_{i,\text{st}}$ are maximally overlapped and stratus liquid water content (LWC)–ice water content (IWC) are uniformly distributed within the single stratus fraction $a_{\text{st}} = \max(a_{l,\text{st}}, a_{i,\text{st}})$; and 3) stratus only fills the noncumulus portion within each grid layer. The third assumption comes from the consideration of distinct properties of turbulent eddies within cumulus and stratus: a convective updraft grows vertically in a nonlocal

way, so that any stratus in its vertical path will be displaced by the convective updraft. These assumed horizontal overlap structures allow us to compute physical stratus fractions, which are passed into various physics schemes and used for numerical computations. If a denotes the four cloud fractions computed in Eqs. (1)–(4), the physical cloud fraction A of each cloud fraction a becomes

$$A_{\text{sh}} = a_{\text{sh}} \leq 0.2,$$

$$A_{\text{dp}} = a_{\text{dp}} \leq 0.6,$$

$$A_{\text{cu}} = A_{\text{sh}} + A_{\text{dp}} \leq 0.8,$$

$$A_{l,\text{st}} = (1 - A_{\text{cu}})a_{l,\text{st}} \leq 1,$$

$$A_{i,\text{st}} = (1 - A_{\text{cu}})a_{i,\text{st}} \leq 1,$$

$$A_{\text{st}} = \max(A_{l,\text{st}}, A_{i,\text{st}}) \leq 1, \quad \text{and}$$

$$A_{\text{tot}} = A_{\text{st}} + A_{\text{cu}} \leq 1, \tag{5}$$

and we reiterate that $\overline{u}_l$ and $\overline{v}_i$ are the grid-mean RH averaged over noncumulus areas in each grid layer.

2) VERTICAL OVERLAP

In CAM5, the following physical processes make use of the vertical overlap structure of clouds and precipitation areas: 1) deep and shallow convection schemes to compute evaporation rates of convective precipitation, 2) aerosol activation, 3) stratiform microphysics to compute production and evaporation rates of stratiform precipitation, 4) wet scavenging (or deposition) of aerosols by convective and stratiform precipitation, and 5) the radiation scheme. While the methods used to compute cloud properties (A, $\hat{q}_l$, $\hat{q}_i$, $\hat{n}_l$, $\hat{n}_i$) and horizontal cloud overlap structure are substantially revised, vertical overlap structures of clouds and precipitation areas in CAM5 are similar to those of CAM3 and CAM4 as summarized below:

- For computing evaporation rates of convective precipitation, the deep and shallow convection schemes assume that the convective precipitation area is 1.
- The aerosol activation routine assumes a maximum vertical overlap of A_{st} between any adjacent layers.
- Stratus microphysics assumes that 1) A_{st} is maximally overlapped in the vertical regardless of vertical separation distance and 2) the stratiform precipitation area $A_{p,\text{st}}$, with nonzero stratiform precipitation flux, is the maximum A_{st} in the layers above the current layer: that is, $A_{p,\text{st}}(k) = \max[A_{\text{st}}(1), A_{\text{st}}(2), \ldots, A_{\text{st}}(k-1)]$, where $k = 1$ is the model top layer.

- Wet scavenging of aerosols consists of two processes: 1) scavenging of activated aerosols within cloud droplets (i.e., cloud-borne aerosols) by precipitation production and 2) scavenging of the remaining nonactivated aerosols (i.e., interstitial aerosols) by precipitation flux falling into the layer. These two processes are separately applied for each form of convective and stratiform precipitation. For the purpose of wet scavenging of aerosols, CAM5 assumes that 1) the convective precipitation area $A_{p,\mathrm{cu}}$ is the vertical integral of A_{cu} in the layers above, weighted by the net production rate of convective precipitation, with similar computation for the stratiform precipitation area, and 2) for computing wet scavenging of nonactivated aerosols, $A_{p,\mathrm{cu}}$ and $A_{p,\mathrm{st}}$ are randomly overlapped with clouds in the layer below. When precipitation is evaporated, some aerosols within the precipitation are redeposited into the atmosphere in proportion to the ratio of the evaporation rate to the precipitation flux falling into the layer.

- Within each grid layer, the CAM5 radiation scheme sees a single total cloud fraction (A_{tot}) and horizontally homogeneous $\hat{q}_{l,\mathrm{tot}}$ and $\hat{q}_{i,\mathrm{tot}}$ within A_{tot}, obtained by cloud area weighting [$\hat{q}_{l,\mathrm{tot}} = (A_{\mathrm{sh}}\hat{q}_{l,\mathrm{sh}} + A_{\mathrm{dp}}\hat{q}_{l,\mathrm{dp}} + A_{\mathrm{st}}\hat{q}_{l,\mathrm{st}})/A_{\mathrm{tot}}$ and similarly for $\hat{q}_{i,\mathrm{tot}}$]. Then, by assuming a maximum–random vertical overlap of A_{tot}, CAM5 generates a set of subcolumns in which the cloud fraction is either 1 or 0 in each layer. Except for cloud condensate, all the other tracers and thermodynamic scalars are assumed to be horizontally homogeneous within each grid layer. By averaging each subcolumn's radiative heating rate, the radiation scheme computes the grid-mean radiative heating profiles.

In principle, all of the above five processes should use the same vertical overlap structure of cloud and precipitation areas. Because of the contrasting nature of the associated turbulent eddies, cumulus and stratus are likely to have different vertical cloud overlap: if vertical shear of the horizontal wind is neglected, cumulus fractions are likely to be maximally overlapped over the entire depth of convective updrafts, while the vertical distance over which stratus is maximally overlapped is likely to be much smaller than for the cumulus. We hope to include these improvements in future versions of CAM.

3. Simulations

Two types of global simulations—1) a stand-alone simulation forced by the observed climatological sea surface temperature (SST) and sea ice fraction with an annual cycle in the year 2000 for 10 yr and 2) a fully coupled simulation without any flux correction between atmosphere and underlying surfaces for 156 yr from 1850 to 2005—are performed at a horizontal resolution of 1.9° latitude × 2.5° longitude with a model physics time step $\Delta t = 1800\,\mathrm{s}$ for both CAM5 at L30 (where L denotes the number of vertical layers) and CAM4 at L26. The fully coupled models (or simulations) with CAM5 and CAM4 will be referred to as the Community Earth System Model, version 1 (CESM1) and the Community Climate System Model, version 4 (CCSM4), respectively. The detailed configurations of the stand-alone and fully coupled simulations as well as other frequently used global simulations [i.e., Atmospheric Model Intercomparison Project (AMIP) and slab-ocean model (SOM) simulations] are described in appendix B. [Except for Figs. 11 and 12, which are from the fully coupled simulations (note that computation of the surface heat flux feedback parameter in Fig. 12 requires the fully coupled simulations), we use the stand-alone simulations for all the analysis in this paper.]

a. CRF

Figure 3 shows CAM5-simulated SW and LW cloud radiative forcings (CRFs) at the top of atmosphere (TOA) compared with the Clouds and the Earth's Radiant Energy Systems Energy Balanced and Filled (CERES-EBAF; Loeb et al. 2009) satellite observations. CRF is the difference of net downward radiative flux between all sky and clear sky, and can be defined at any height, with positive (negative) CRF indicating that the cloud warms (cools) the underlying atmosphere and surface. For references, CAM5-simulated global annual-mean net downward SW radiation at TOA and upward LW radiation at the top of the model are 242.2 and 237.7 W m^{-2}, respectively.

One important caveat in comparing CAM5-simulated CRFs with the observations is that CAM5-simulated CRFs are computed by assuming that all thermodynamic variables (e.g., water vapor, temperature, and concentrations of gases and aerosols), except the mass and number concentration of cloud condensates are horizontally uniform within each grid layer. This assumption inevitably overestimates $q_{v,\mathrm{clr}}$ (water vapor in the clear portion that is set to the grid-mean $\overline{q}_v$ in CAM5) as cloud fraction increases {i.e., $\Delta q_{v,\mathrm{clr}} \equiv q_{v,\mathrm{clr}}^{\mathrm{CAM5}} - q_{v,\mathrm{clr}}^{\mathrm{OBS}} = [a/(1-a)](q_{v,s} - \overline{q}_v) > 0$, where $q_{v,\mathrm{clr}}^{\mathrm{CAM5}} = \overline{q}_v$, $q_{v,\mathrm{clr}}^{\mathrm{OBS}} = q_{v,\mathrm{clr}}, \overline{q}_v = aq_{v,s} + (1-a)q_{v,\mathrm{clr}}, a$ is cloud fraction, and $q_{v,s}$ is saturation specific humidity in the cloudy portion}. Since water vapor reduces the atmospheric emission temperature and so increases the amount of net downwelling LW radiation, CAM5-simulated LW CRF will be underestimated relative to the observations estimated for cloud free pixels, especially in the regions where clouds are abundant, even if CAM5 perfectly simulates cloud properties and the vertical overlap of
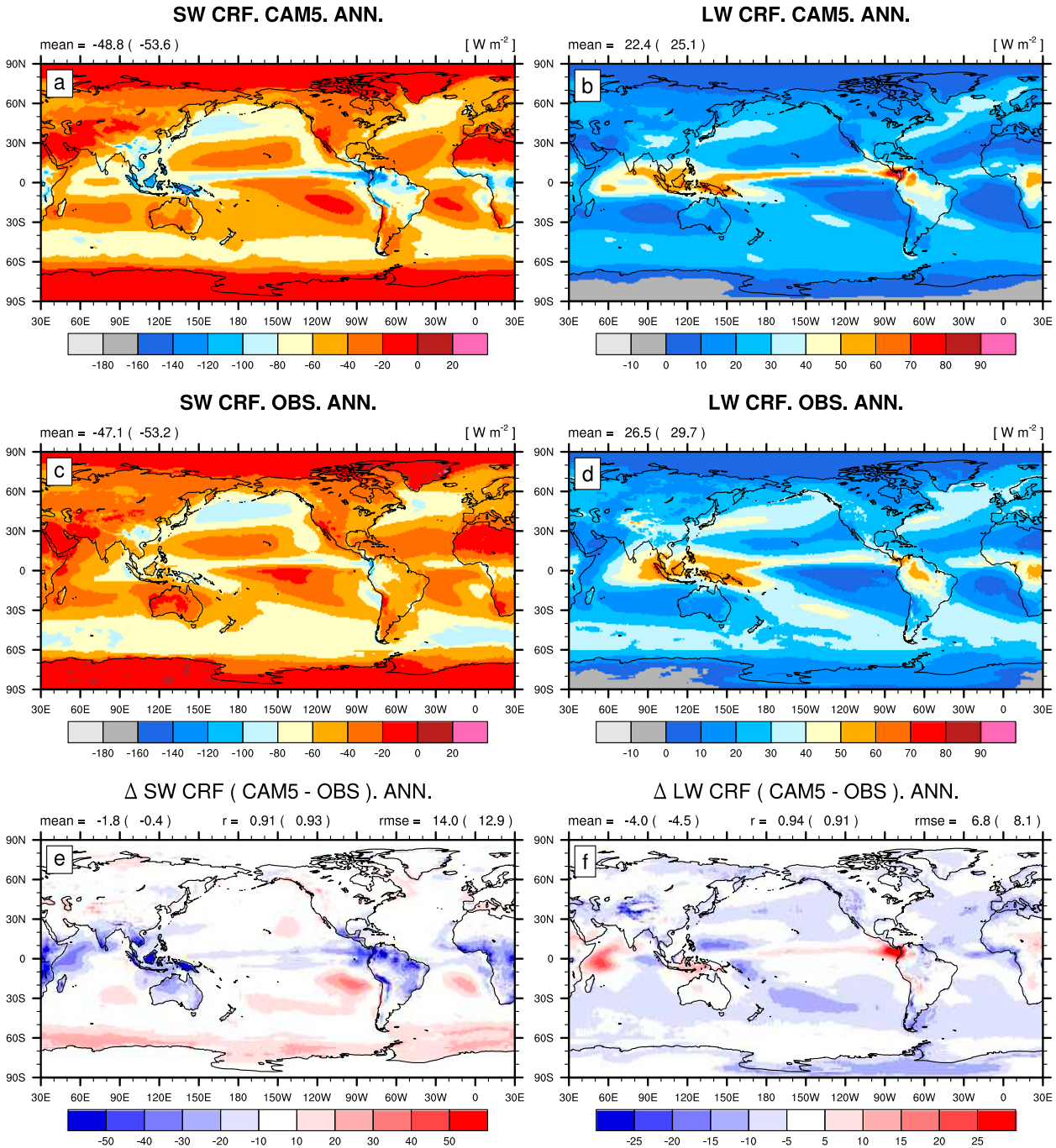
FIG. 3. Annual-mean (left) SW and (right) LW CRF at the TOA from (top) CAM5 and (middle) observations (OBS). (bottom) The difference maps between CAM5 and OBS obtained by converting the CAM5 simulation into the horizontal grid of the observation with appropriate area weighting. The area-weighted global-mean value is denoted by mean at the top left of individual plots with corresponding unit and color scales at the top right and bottom of each plot, respectively. In (bottom), r and rmse at the top of each plot denote global pattern correlation and root-mean-square error between CAM5 and OBS. The observation is the 10-yr climatology of CRF from CERES-EBAF (March 2000–February 2010; Loeb et al. 2009). The same global-mean statistics of CRFs at SFC from CAM5 and the ISCCP-derived surface radiative flux data (January 1984–December 2007: 17 yr; Zhang et al. 2004) are also denoted in the parenthesis at the top of each plot. Similar plotting rules are used in the following horizontal 2D plots.

clouds. Ideally, the radiation scheme should handle the horizontal heterogeneity of q_v (and temperature and concentrations of gases and aerosols, if possible) within each grid layer.

CAM5-simulated global annual-mean SW CRF at TOA is $-48.8\,\text{W\,m}^{-2}$, which is within the range of available satellite observations [$-47.1\,\text{W\,m}^{-2}$ from CERES-EBAF as shown in Fig. 3c and $-54.2\,\text{W\,m}^{-2}$ from the Earth Radiation Budget Experiment (ERBE; Harrison et al. 1990)]. Overall, CAM5 successfully captures the observed regional maxima of SW CRFs over the following three main cloud regimes with a global pattern correlation $r = 0.91$ between CAM5 and observations: 1) the tropical deep convection regime, 2) subtropical marine stratocumulus decks on the west of the major continents, and 3) midlatitude oceans. As shown in Fig. 3e, CAM5 has systematic regional biases of SW CRF at TOA [root-mean-square error (rmse) = $14.0\,\text{W\,m}^{-2}$], although they are smaller than the corresponding biases in CAM4 (rmse = $17\,\text{W\,m}^{-2}$): 1) substantial overestimation (i.e., more cooling) in the tropical deep convection regime, especially over the continents; 2) underestimation over the eastern subtropical oceans downstream of marine stratocumulus decks and over the portion of midlatitude oceans with strong meridional SST gradient, where downwind transition between stratocumulus and cumulus widely occurs; 3) underestimation over the Southern Hemispheric circumpolar ocean (SHC) poleward of 55°S mainly during December–February (DJF); and 4) underestimation by more than $20\,\text{W\,m}^{-2}$ over the Arctic during June–August (JJA; although not so evident in the annual mean). CAM5-simulated global annual-mean SW CRF at the surface (SFC) is nearly identical to observations (Δmean = $-0.4\,\text{W\,m}^{-2}$) and the regional bias patterns at SFC are very similar to those at TOA (not shown).

The CAM5 tuning strategy is to minimize the overall climate bias score measured by the average time–space rmse errors of several semi-independent key thermodynamic variables (see Park and Bretherton 2009) while satisfying a couple of mandatory conditions (global energy balance at the top of the model and stable coupled simulation) and improving specific phenomena that are important for climate research but are not well simulated (e.g., ENSO and an acceptable magnitude of aerosol direct and indirect effects). Because CAM5's physics–dynamics schemes are not perfect, some aspects such as SW CRF are inevitably biased under our tuning strategy.

CAM5-simulated global annual-mean LW CRF at TOA is $22.4\,\text{W\,m}^{-2}$, significantly smaller than the available observations ($26.5\,\text{W\,m}^{-2}$ from CERES-EBAF as shown in Fig. 3d and $30.4\,\text{W\,m}^{-2}$ for ERBE). A similar underestimate can be seen in the LW CRF at SFC

($\Delta\text{LWCRF}_{\text{SFC}} \equiv \text{LWCRF}_{\text{SFC}}^{\text{CAM5}} - \text{LWCRF}_{\text{SFC}}^{\text{OBS}} = -4.5\,\text{W\,m}^{-2}$; $\Delta\text{LWCRF}_{\text{TOA}} = -4.0\,\text{W\,m}^{-2}$). Based on the fact that CAM5 simulates a realistic magnitude of global annual-mean SW CRF, we speculate that CAM5's underestimation of global annual LW CRFs may be partly due to the setting of $q_{v,\text{clr}} = \overline{q}_v$ in the radiation scheme. If a correct $q_{v,\text{clr}} = (\overline{q}_v - aq_s)/(1 - a)$ was used, CAM5-simulated LW CRF would be larger than that shown in Fig. 3b, especially in regions where the vertical integral of $\Delta q_{v,\text{clr}}$ is large. One of other contributors that are probably larger is too high column precipitable water (which leads to too much clear-sky greenhouse and thus tends to reduce the LW CRF).

With this caveat in mind, CAM5 overestimates LW CRF in the tropical deep convection regimes over the western coast of Central America and the intertropical convergence zone (ITCZ), the western Indian Ocean, and Africa. With opposite signs, these regional biases are roughly consistent with the biases in the SW CRF at TOA, implying that CAM5 simulates too much (or too optically thick or too high) upper-level clouds in the tropical deep convection regimes. The biases of LW CRF at TOA over the eastern subtropical stratocumulus-to-cumulus transition regimes and the SHC ocean are much weaker than the corresponding biases in SW CRF, implying that CAM5 simulates too few (or too optically thin) low-level clouds there. In section 3j, we discuss possible sources of these regional biases in SW and LW CRFs at the process level. The net radiative impact of clouds on the global atmospheric column (not the sum of the atmospheric column and underlying surface) is a warming, with a global annual mean of $2.1\,\text{W\,m}^{-2}$ in CAM5 (SW warming = 4.8; LW cooling = 2.7) and $2.9\,\text{W\,m}^{-2}$ from observations (SW warming = 6.1; LW cooling = 3.2).

b. Cloud fraction and cloud condensate amount

SW CRF is a function of cloud fraction and cloud optical thickness, which in turn is a function of cloud LWC/IWC and cloud droplet radius. Cloud-top temperature also plays an important role in LW CRF. To obtain insight into the biases of CAM5-simulated CRFs, we plot the total cloud fraction (CLDTOT) and column-integrated LWC (TGCLDLWP; which includes both stratus and cumulus LWPs) in Fig. 4.

Overall, CAM5-simulated CLDTOT is similar to the International Satellite Cloud Climatology Project (ISCCP; Rossow and Schiffer 1991) observations with a global annual-mean CLDTOT of 63% (observation = 66.8%), $r = 0.94$, and rmse = 10.5%. Both CAM5 and observations show maximum CLDTOTs in the tropical deep convection and midlatitude oceans, which project onto both SW and LW CRFs. However, the maximum
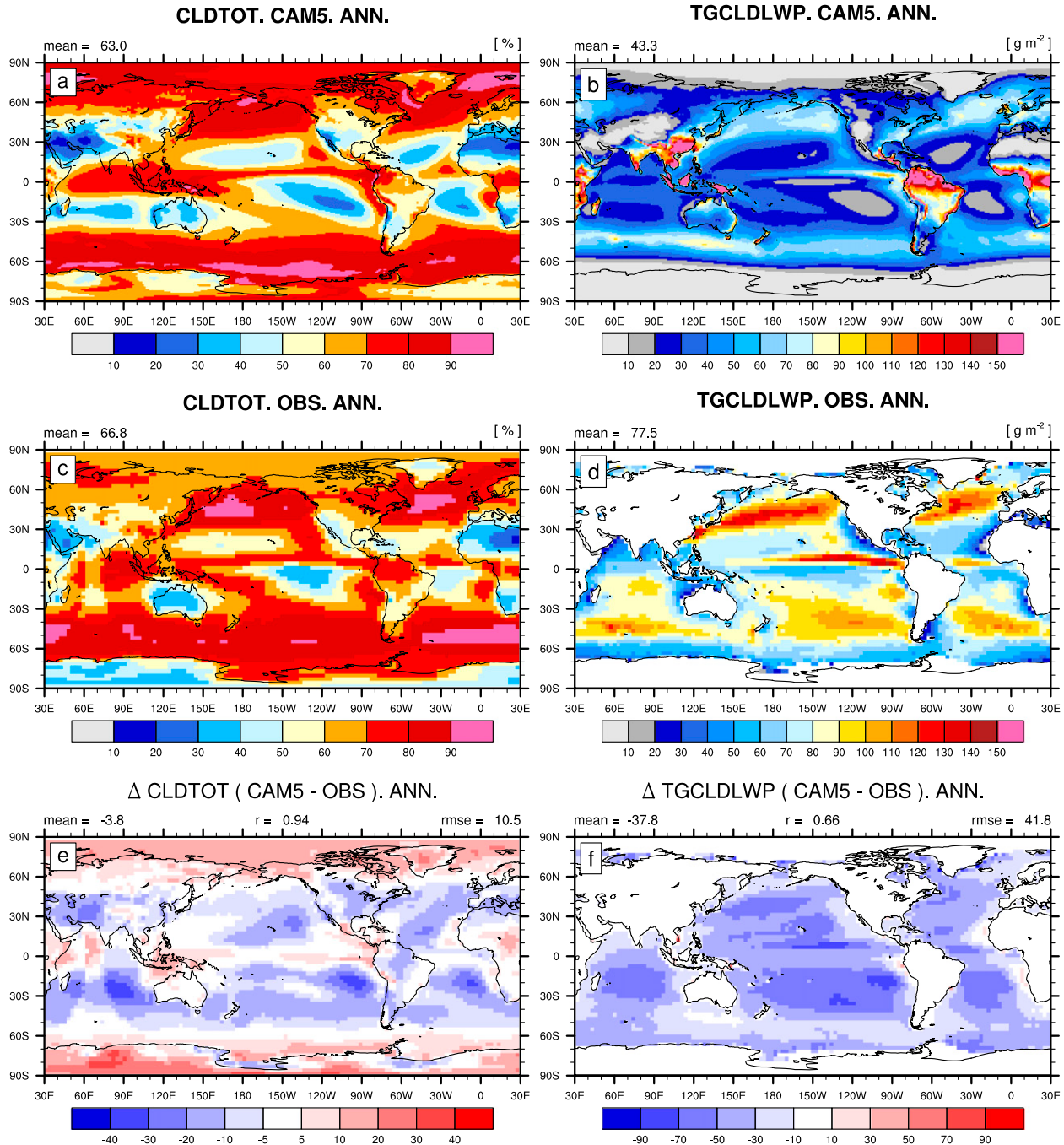
FIG. 4. As in Fig. 3, but for the annual-mean (left) CLDTOT and (right) TGCLDLWP. The observations are the 19-yr climatology of infrared-based total cloud fraction from the ISCCP D2 (July 1983–December 2001; Rossow and Schiffer 1991) and the 12-yr climatology of column-integrated grid-mean cloud LWC over the ocean from the NVAP (January 1988–December 1999; Randel et al. 1996). The global-mean statistics are only over the ocean in (d),(f). Note that vertical overlapping assumptions used for computing CLDTOT as well as the definition of cloud in each layer differ between CAM5 and OBS.

CLDTOT over the eastern subtropical oceans are projected only onto SW CRF and not LW CRF, indicating lower-tropospheric clouds. The maximum CLDTOT in the Arctic is not evident in either CRF, probably because the underlying surface (sea ice or snow) is as reflective as clouds and the typical cloud-top temperature is comparable to that of the surface. CAM5-simulated CLDTOT is 1) overestimated over the tropical deep convection regime, 2) underestimated over the eastern subtropical oceans downstream of marine stratocumulus

decks, and 3) overestimated over the polar regions. These biases exist throughout the year with the first (second) bias being projected on both CRFs (SW CRF). Over the Arctic in JJA, CAM5 overestimates CLDTOT by 15%, but underestimates SW CRF cooling more than $20 \, \text{W m}^{-2}$ (CAM5-simulated clear-sky surface albedo is smaller than the observations). Over the SHC ocean during DJF, CAM5-simulated CLDTOT is similar to observations, but SW CRF cooling is underestimated by more than $50 \, \text{W m}^{-2}$. This indicates that over the summer Arctic and the SHC ocean, CAM5-simulated in-cloud condensate is much smaller (or droplet radius is much larger) than the observations, as is also reflected in the negative biases of TGCLDLWP in the SHC ocean (Fig. 4f).

CAM5-simulated global annual-mean TGCLDLWP is $43.3 \, \text{g m}^{-2}$ with distinctively high values over tropical land areas and China. Since TGCLDLWP is a function of cloud fraction, the global pattern of TGCLDLWP is roughly similar to CLDTOT, but with larger values in the midlatitude oceans, where stratus LWP in the lower and midtroposphere mostly contributes (Figs. 8g and 9h). When averaged over the ocean, CAM5-simulated TGCLDLWP is only half of the observed $77.5 \, \text{g m}^{-2}$ from the National Aeronautics and Space Administration (NASA) Water Vapor Project (NVAP; Randel et al. 1996). Except near the coasts, CAM5 underestimates TGCLDLWP all over the oceans throughout the year, with pronounced maximum negative biases over the eastern subtropical oceans and a portion of midlatitude oceans where meridional SST gradient is large. The biases over the subtropical and midlatitude oceans are consistent with the corresponding biases of CLDTOT and SW CRF, indicating CAM5 does not generate enough cloud condensate there. Section 3j will provide a discussion on the sources of these biases of CLDTOT and TGCLDLWP.

c. Precipitation rate at the surface

Figure 5 shows the CAM5-simulated annual-mean total (convective + stratiform) precipitation rate at the surface compared with the Climate Prediction Center (CPC) Merged Analysis of Precipitation (CMAP; Xie and Arkin 1996). The observed climatologies and CAM5 biases of total precipitation rates in DJF and JJA are shown in the middle and bottom panels of Fig. 6, respectively.

The CAM5-simulated global annual-mean total precipitation rate is $3.01 \, \text{mm day}^{-1}$, about 12%–15% larger than the satellite-derived observational estimates [$2.69 \, \text{mm day}^{-1}$ for CMAP during 1979–98 and $2.61 \, \text{mm day}^{-1}$ for the Global Precipitation Climatology Project (GPCP; Huffman et al. 2009) during 1979–2003].
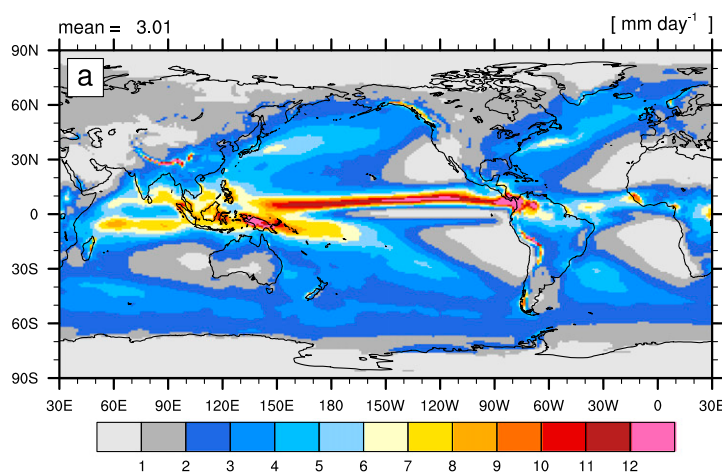
Stephens et al. (2012) suggested these satellite estimates may be biased low, which would reduce most of the discrepancy. While the overall patterns are similar ($r = 0.93$), systematic regional biases can be identified in CAM5 simulation (and also in the CAM4 simulation): 1) too strong precipitation along the ITCZ extending to the west coast of Central America, especially in DJF; 2) a double ITCZ over the eastern tropical Pacific Ocean south of the equator, especially in DJF; 3) too strong precipitation over the great mountain areas of the Himalayas (especially in JJA), the Andes (especially in DJF), and the Rockies; 4) anomalous precipitation over the desertlike southern portion of the Arabian peninsula in JJA; 5) a meridional shift of the Atlantic ITCZ extending into Africa; 6) complex regional biases over the western tropical Pacific warm pool and Indian Ocean with strong seasonality; and 7) positive biases over the midlatitude storm track, especially during boreal winter. The same comparison against the GPCP instead of the CMAP observation shows similar bias patterns, except that the positive biases in the tropical (extratropical) regions are enhanced (reduced) (not shown).

In CAM5, two types of precipitation exist: convective precipitation (a sum of deep and shallow convective precipitation) generated by single-moment convective microphysics and stratiform precipitation generated by double-moment stratiform microphysics. In this 1.9° latitude × 2.5° longitude horizontal resolution simulation, CAM5-simulated precipitation in the tropics (midlatitude storm track) is mostly convective (stratiform), with similar contributions from both convective and stratiform precipitation over the Himalayas and the Andes (top panels of Fig. 6). The global ratio of the shallow convective precipitation rate to the deep convective precipitation rate simulated by CAM5 is about 0.2 (not shown).
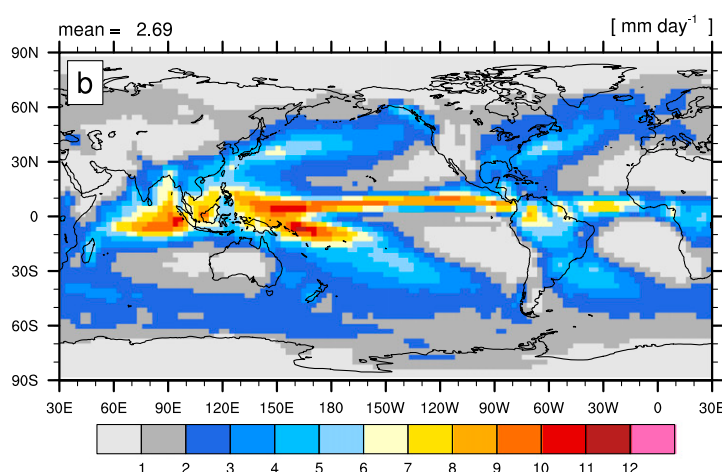
d. The frequencies of deep and shallow cumulus

Figure 7 shows the CAM5-simulated annual-mean frequency of occurrence (FQ) of deep and shallow cumulus compared with surface observations estimated using the methodology described in Park and Leovy (2004). The definitions of individual cumulus FQs from CAM5 and surface observations are given in the caption of Fig. 7. We repeated the same analysis by changing the definitions of CAM5-simulated shallow and deep cumulus (e.g., 0.001 instead of 0.01 as the threshold of saturated updraft fraction, 880 and 850 hPa instead of 900 hPa as the reference level of shallow cumulus, and 450 and 350 hPa instead of 400 hPa as the reference level of deep cumulus), but the results were qualitatively similar to those shown in Fig. 7.
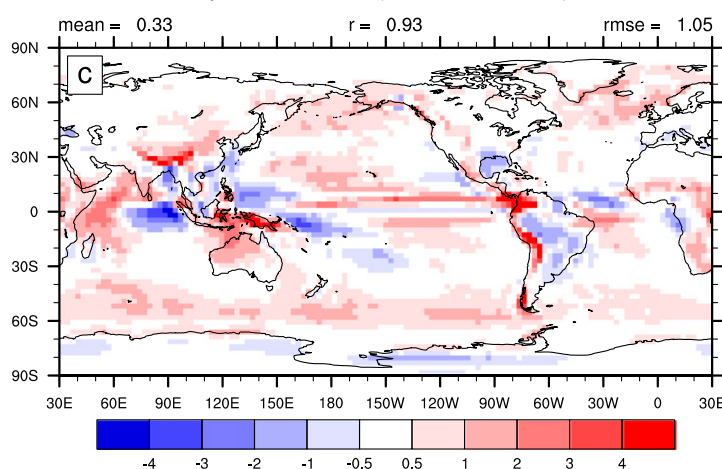
FIG. 5. As in Fig. 3, but for the annual-mean precipitation rate at the surface. The observations are 20-yr climatologies of surface precipitation rates from CMAP (January 1979–December 1998; Xie and Arkin 1996).
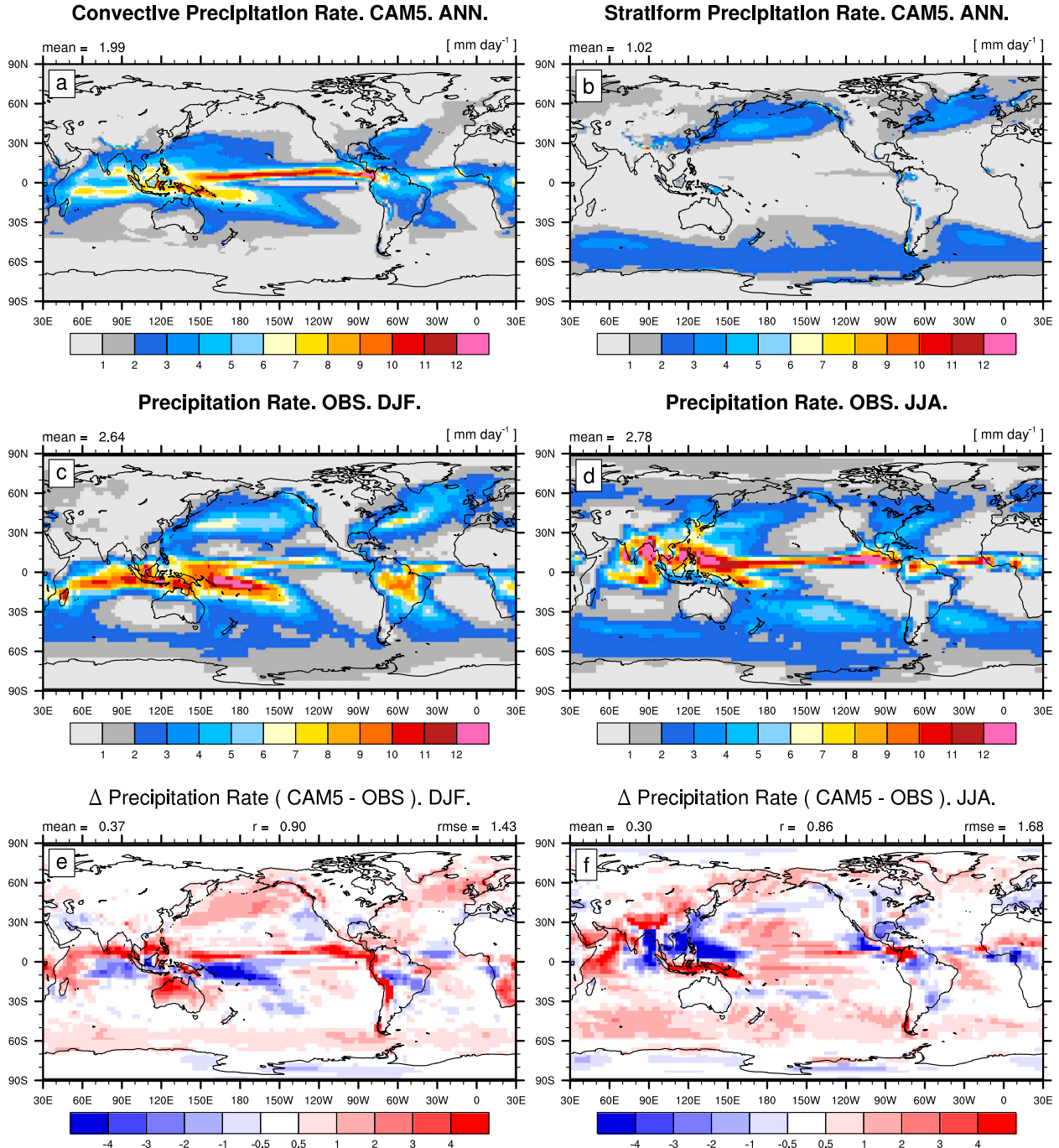
FIG. 6. (top) CAM5-simulated annual-mean convective and stratiform precipitation rates at the surface; (middle) observed precipitation rates at the surface from CMAP in DJF and JJA; and (bottom) the difference maps of surface precipitation rates between CAM5 and OBS in DJF and JJA.

The global pattern correlations between CAM5 and observations are $r = 0.64$ for deep cumulus FQ and $r = 0.81$ for shallow cumulus FQ. CAM5-simulated deep cumulus is mostly concentrated in the tropics, with a negative bias over the subtropical trade cumulus region throughout the year, the northeastern Atlantic and

northwestern Pacific Oceans in DJF, and northern Asia and the SH midlatitude ocean during JJA. In the tropical deep convection regions, CAM5 overestimates deep cumulus FQ substantially over land during boreal summer. Some care is needed in the interpretation of these biases because of differences in the method used to
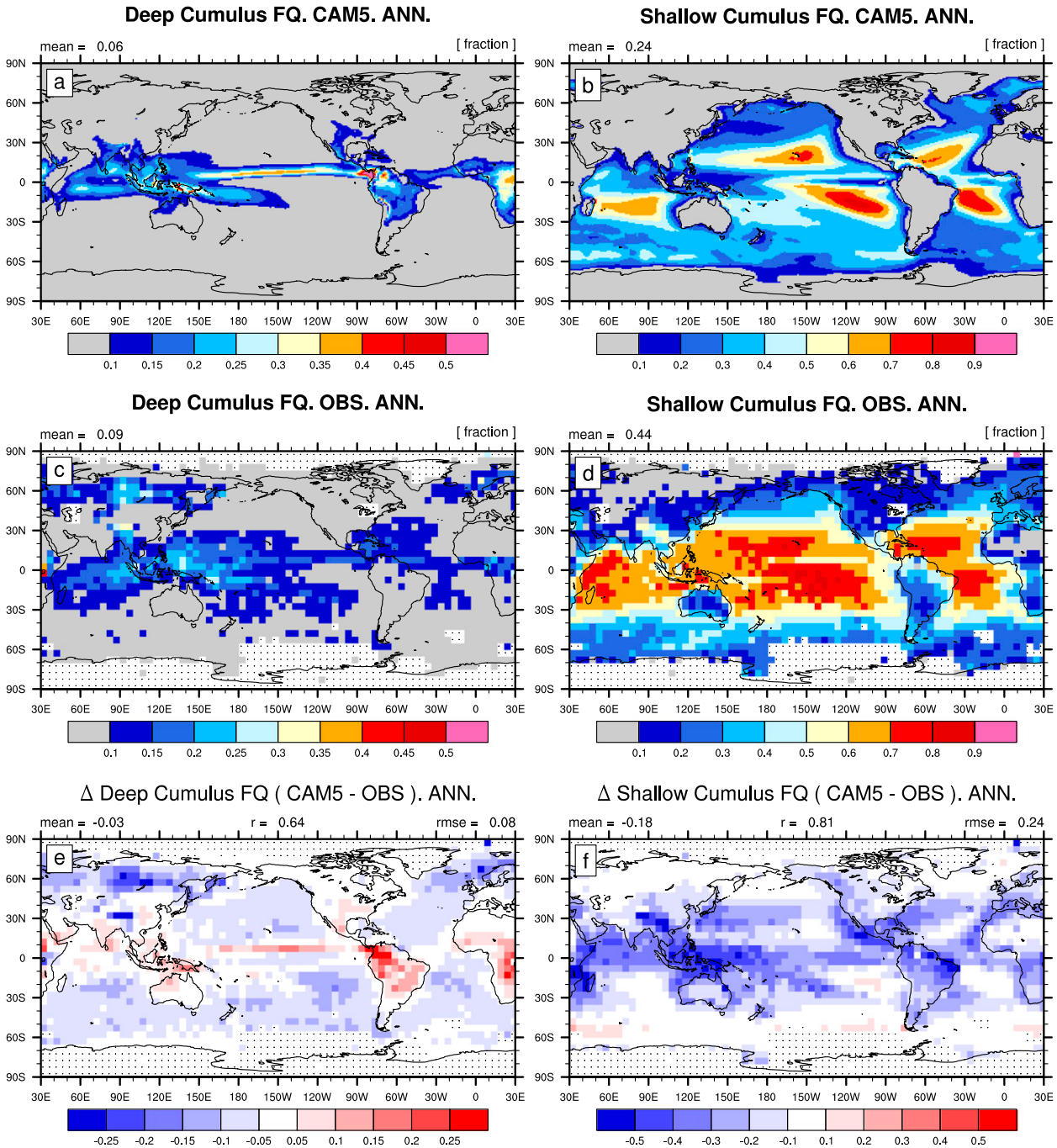
FIG. 7. As in Fig. 3, but for the annual-mean frequencies of (left) deep cumulus and (right) shallow cumulus (FQ). The observations are the 53- and 26-yr climatologies of low-cloud FQs over ocean/land at 5° latitude × 5° longitude computed from the Extended Edited Cloud Report Archive (EECRA; Hahn and Warren 1999). In the case of simulations, deep (shallow) cumulus FQ is defined as the fractional occurrence of saturated deep (shallow) cumulus with updraft fractional area larger than 0.01 at 400 (900) hPa. The observed deep (shallow) cumulus FQs are defined as the ratio of the number of observations that reported low-cloud type of CL = 3 or 9 (CL = 1, 2, 4, and 8) to the total number of observations that reported any low-cloud-type information. The method used for computing the observed climatological FQs of various cloud types from individual surface observations is detailed in Park and Leovy (2004). In (c)–(f), grid boxes without enough observations to form a reasonable climatology are regarded as missing and denoted with a dot and global-mean statistics are computed using only the nonmissing grids.

produce the FQs between the model and observations. However, from the consistent positive biases of the tropical CRFs (Fig. 3), we speculate that overly frequent tropical deep convective frequency in CAM5 may be real. This may be associated with the assumption that deep convection occurs whenever CAPE exceeds a threshold, and the specification of a CAPE relaxation time scale of $\tau = 1$ h (greater than the model integration time step $\Delta t = 1800$ s), which requires more frequent convective events to neutralize atmospheric static instability. This aspect should be explored more in the future.

Except for some regions of the trade cumulus region and the SH midlatitude ocean during DJF, CAM5-simulated shallow cumulus FQ is smaller than the observed estimates with significant negative biases in the tropical deep convection regimes and over summer continents (e.g., over the central United States in JJA, the observed shallow cumulus FQ is about 30% while CAM5 is less than 10%). This may be an artifact of the process splitting in CAM5 described in Fig. 1. Because the deep convection parameterization stabilizes the column before the shallow convection parameterization is invoked, shallow convection will occur less often than it would otherwise. On the other hand, the higher reporting priority given to deep cumulus (CL = 3 and 9) over shallow cumulus (CL = 1, 2, 4, and 8; see Park and Leovy 2004) makes the shallow cumulus FQ reported by surface observers smaller than reality. Since there is no way to quantify the effects of these two artificial factors (e.g., process splitting versus reporting priority), we avoid further interpretation of the negative biases of shallow cumulus FQ in the tropical convective systems that usually accompany both deep and shallow cumulus. However, the negative biases of shallow cumulus FQ over North America during summer may be real, reflecting that CAM5 fails to capture forced convection [i.e., convective updrafts that reach the LCL but not to the level of free convection (LFC)] since both the CIN closure in the shallow convection scheme and the CAPE closure in the deep convection scheme are designed to simulate only the positively buoyant convective updrafts growing above the LFC (i.e., free convection). In the subtropical trade cumulus regime, CAM5-simulated shallow cumulus FQ is roughly similar to observations, even though substantial negative biases of SW CRF, CLDTOT, and TGCLDLWP exist there.

e. LWP and IWP from individual cloud types

Within each grid layer, CAM5 generates deep and shallow cumulus and stratus, which are assumed to occupy horizontally nonoverlapped regions, each with its own cloud fraction, in-cloud LWC/IWC and droplet radius [Eq. (5)]. Figure 8 shows the contribution of each of these three cloud types to TGCLDLWP (left panels) and TGCLDIWP (right panels). In this plot, cumulus LWP/IWP are not the detrained convective condensate but the in-cumulus condensate within the quasi-steady convective updraft plumes that are used only for radiation computation, without being advected by grid-mean flow. In the global annual average, 65% (23% and 12%) of LWP comes from stratus (deep cumulus and shallow cumulus) with similar partitioning for IWP (62%, 22%, and 16%, respectively) but with slightly larger (smaller) contribution from shallow cumulus (stratus).

In the tropical regions, deep cumulus LWP/IWP over land are generally larger than over ocean, due partly to the use of smaller autoconversion efficiency (c_0) of deep cumulus condensate into convective precipitation over land ($c_{0,\text{lnd}} = 0.0059$ m^{-1} and $c_{0,\text{ocn}} = 0.045$ m^{-1}), although this may be also due to the stronger buoyancy flux over land tied to the diurnal cycle. Some in-cumulus condensate within deep convective updrafts is detrained in the layers above the level of minimum grid-mean moist static energy and becomes a part of stratus condensate after evaporation and sublimation. Larger stratus LWP/IWP over tropical land than ocean partially reflects the larger amount of detrained deep cumulus condensate over land. However, very large stratus LWP over China might also be enhanced with abundant surface aerosol emission that suppresses stratiform precipitation by reducing the radius of stratus liquid droplets there. A sensitivity simulation with the preindustrial aerosol emission produced smaller LWP than the simulation with the present-day aerosol emission over China (not shown).

Although shallow cumulus LWP is small, it is broadly distributed over subtropical and midlatitude oceans and exerts radiative impacts. At (20°N, 150°W), east of Hawaii, CAM5-simulated shallow cumulus FQ is at a maximum (Fig. 7b), and shallow cumulus LWP is 20 g m^{-2}, larger than stratus LWP (<10 g m^{-2}). Even with the inclusion of the radiative effects of the cumulus updrafts, however, CAM5-simulated SW CRF is smaller than observations (Fig. 3e) in association with negative biases of CLDTOT and TGCLDLWP there (Figs. 4e,f). This implies that penetrative entrainment drying at the cumulus top is stronger than upward moisture transport from the sea surface, resulting in the dissipation of overlying stratocumulus. The sensitivity of the CAM5 cloud system to the penetrative entrainment efficiency will be discussed in section 3j. Shallow cumulus LWP is also at a maximum on the northern flank of the SST cold tongue over the eastern equatorial Pacific Ocean. During August–October along 95°W, stratus, shallow cumulus, and deep cumulus LWP reaches a maximum at
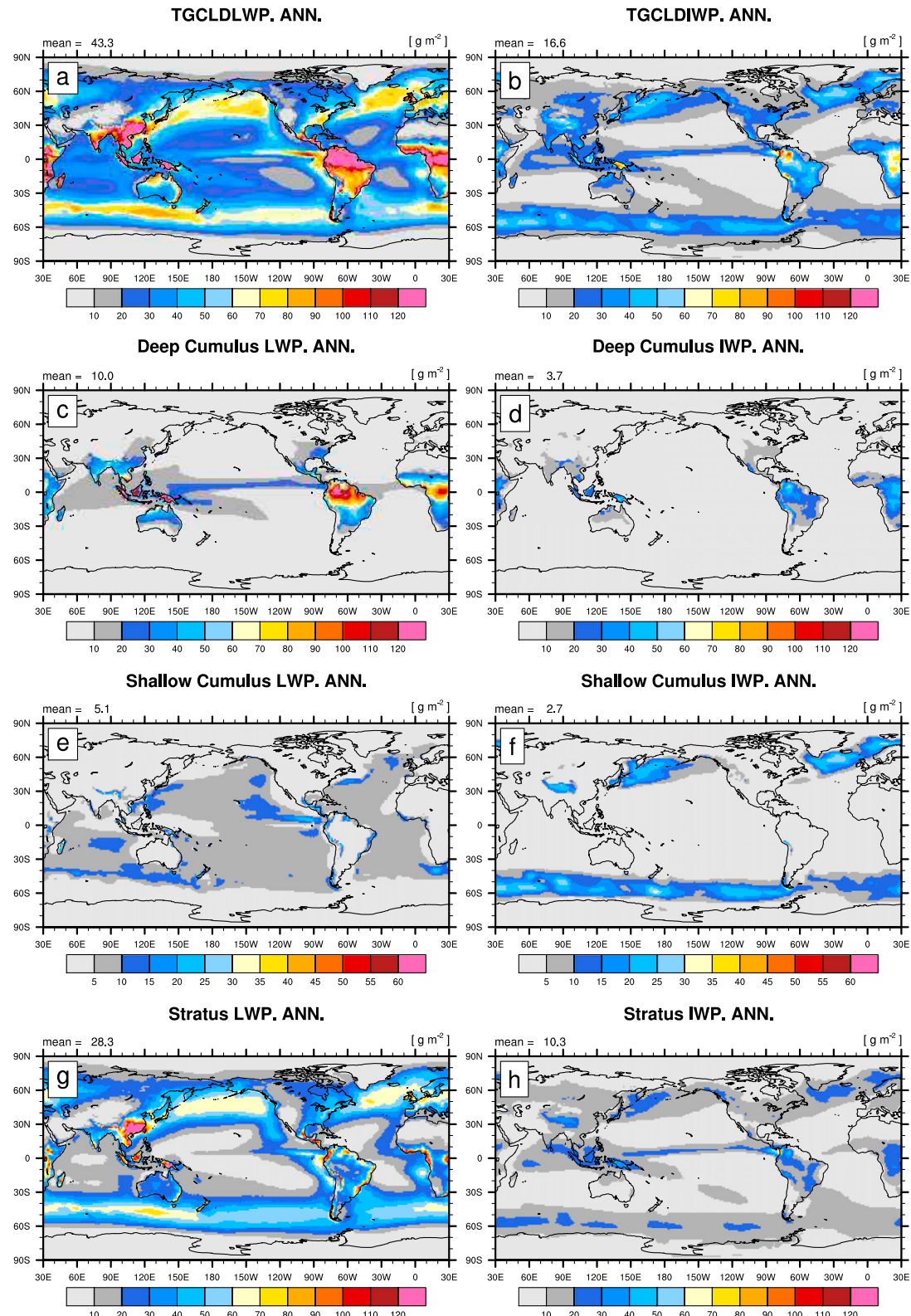
FIG. 8. CAM5-simulated annual-mean (left) column-integrated LWC and (right) column-integrated IWC from (a),(b) all types (deep cumulus + shallow cumulus + stratus) of clouds (TGCLDLWP and TGCLDIWP); (c),(d) deep cumulus; (e),(f) shallow cumulus; and (g),(h) stratus.

3°, 5°, and 7°N, respectively, in response to the changes of PBL structures in the vicinity of the SST cold tongue and grid-mean vertical velocity.

In the extratropical regions, most TGCLDLWP comes from stratus with some contribution from shallow cumulus. Along the midlatitude oceanic storm track during boreal winter, shallow cumulus IWP is as large as stratus IWP, indicating the importance of convective updrafts in postfrontal cold air outbreaks. The CAPE closure that is mainly designed for simulating tropical deep convection inhibits the triggering of frontal deep convection in the midlatitude regions (Fig. 7a); therefore, the shallow convection scheme is active instead.

f. Zonal-mean cross sections of cloud properties

Figure 9 shows CAM5-simulated zonal-mean cross sections of in-cloud (with hat) and grid-mean (with overbar) LWC ($\hat{q}_l$ and $\overline{q}_l$ in the first and third rows) and IWC ($\hat{q}_i$ and $\overline{q}_i$ in the second and fourth rows) of cumulus (left column), stratus (center column) and total cloud (right column) with corresponding cloud fractions (A_{cu}, A_{st}, and A_{tot}). Figure 10 also shows $\overline{q}_l$ and $\overline{q}_i$ from shallow and deep cumulus (left column) and effective radius ($\hat{r}_{l,st}$, $\hat{r}_{i,st}$) and number concentrations ($\hat{n}_{l,st}$, $\hat{n}_{i,st}$) of in-stratus liquid droplets and ice crystals (right column) with corresponding cloud fractions (A_{sh}, A_{dp}, $A_{l,st}$, and $A_{i,st}$). All the in-cloud variables denoted by a hat are obtained by averaging only the cases when the corresponding cloud is present.

CAM5-simulated annual zonal-mean $\hat{q}_{l,cu}$ and $\hat{q}_{i,cu}$ ($\hat{q}_{l,st}$ and $\hat{q}_{i,st}$) are less than 0.4 (0.5 and 0.05) g kg^{-1}. CAM5's shallow convection and stratiform macrophysics schemes are constructed in such a way that $\hat{q}_{l,st} + \hat{q}_{i,sh}$ ($\hat{q}_{l,st}$ and $\hat{q}_{i,st}$) is smaller than an upper bound of 0.7 (3.0 and 5.0) g kg^{-1}. In the tropical middle and upper troposphere, CAM5-simulated $\hat{q}_{i,cu}$ is less than 0.1 g kg^{-1}, much smaller than observed values of ~1 g kg^{-1} (Prabha et al. 2011) averaged across deep cumulus. Given that CAM5-simulated deep convective activity occurs too frequently (Fig. 7e) and the empirical Eq. (1) diagnoses a somewhat large deep cumulus fraction (e.g., $a_{dp} \sim 0.2$ if $M_{dp} = 0.01$ kg s^{-1} m^{-2}), CAM5's tuning effort to reduce $\hat{q}_{i,cu}$ by enhancing the autoconversion efficiency c_0 was an inevitable choice necessary to simulate reasonable values for the overall time-mean radiative and hydrological effects of deep convection. Future deep convection schemes should be constructed to produce a more realistic occurrence of convective frequency, a_{dp}, and $\hat{q}_{i,cu}$ in a more consistent way with a built-in feedback among them and without needing obvious compensating errors to match the climatology.

The composite cloud properties provided to the radiation scheme are shown in Figs. 9c,f ($A_{tot} = A_{cu} + A_{st}$,

$\hat{q}_{l,tot} = (A_{cu}\hat{q}_{l,cu} + A_{st}\hat{q}_{l,st})/A_{tot}$, and similarly for $\hat{q}_{i,tot}$). In this way, CAM5 takes into account the radiative effects of cumulus as well as stratus, even though incumulus thermodynamic content is not transported by the grid-mean advection scheme. However, CAM5's use of a single set of cloud variables for the radiation transfer computation will inevitably overestimate grid-mean radiative impacts of clouds, since cloud reflectivity r (or emissivity ϵ for LW radiation) is a nonlinear function of optical thickness: that is, $r = 1 - \exp(-\tau)$ where $\tau = k\rho_{air}\hat{q}_l\Delta z$ is cloud optical thickness, k is the extinction cross section, ρ_{air} is air density, and Δz is cloud thickness. As an example, if cumulus and stratus coexist in a single transparent layer with the properties $A_{cu} = A_{st} = 0.1$, $\hat{q}_{l,cu} = 0.1$ g kg^{-1}, $\hat{q}_{l,st} = 0.5$ g kg^{-1}, $k = 90$ m^2 kg^{-1}, $\Delta z = 100$ m, and $\rho_{air} = 1$ kg m^{-3}, then CAM5-simulated grid-mean reflectivity is $\overline{r}_{CAM5} = 0.19$, larger than the $\overline{r} = 0.16$ computed by taking individual cumulus and stratus into account. Future radiation schemes should be able to handle individual cloud types in each layer. Inhomogeneity of $\hat{q}_l$ and $\hat{q}_i$ within individual cloud types is also a part of this problem. An inhomogeneity factor reducing the $\hat{q}_l$ and $\hat{q}_i$ passed to the radiation scheme is perhaps the most reasonable way to deal with this.

Cumulus exists in a wide range of regions from the tropics to the midlatitudes and from the lower to the upper troposphere (Figs. 9g,j). In the tropics, deep convection grows up to the upper troposphere and stabilizes the atmospheric column, which inhibits shallow cumulus growing above ~800 hPa in the process-splitting CAM5 (Fig. 10a). In the midlatitudes where CAM5-simulated deep convective activity is weak, however, shallow cumulus grows up to ~600 hPa and contributes more than 50% of the $\overline{q}_{i,tot}$ there (Figs. 10c and 9l).

Most of the CAM5-simulated $\overline{q}_{i,st}$ is distributed in the midlatitude storm track throughout the whole troposphere, especially during boreal winter, and also in the tropical–subtropical upper troposphere in all seasons, with a maximum value of 0.01 g kg^{-1} at 250 hPa near the northern equator. In the lower troposphere of the midlatitude storm track, maximum $\overline{q}_{i,sh}$ is collocated with the maximum $\overline{q}_{i,st}$ (Figs. 9k and 10c), implying that some of $\overline{q}_{i,st}$ is generated from the detrained condensate from shallow cumulus, and the other portion of $\overline{q}_{i,st}$ comes from the freezing of $\overline{q}_{l,st}$ (Figs. 9h,k). The deep cumulus top is located just below the maximum $\overline{q}_{i,st}$ in the tropics (Figs. 9k and 10g), implying that detrained deep cumulus condensate is a major source of $\overline{q}_{i,st}$ in the upper troposphere.

CAM5 simulates a maximum $\overline{q}_{l,st}$ at 875 hPa along 45°N/S (Fig. 9h), with a lower maximum $\overline{q}_{l,st}$ in the subtropics where marine stratocumulus decks exist on the western side of the major continents (Fig. 8g) and in
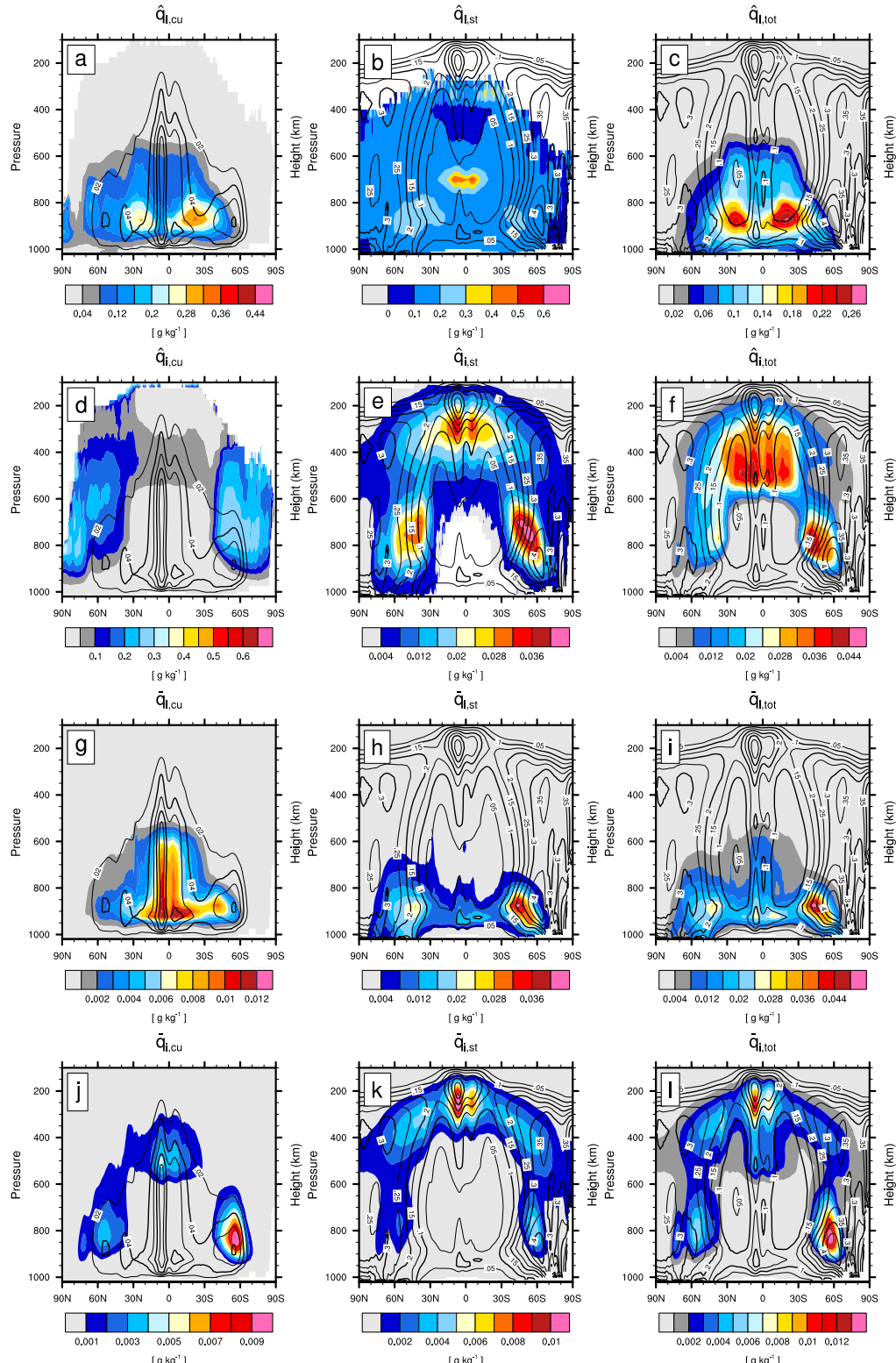
FIG. 9. CAM5-simulated annual zonal-mean cross sections of cloud condensates (color shading) and cloud fractions (solid lines) from (left) cumulus (A_{cu}), (center) stratus (A_{st}), and (right) cumulus + stratus (A_{tot},). Shown are in-cloud (a)–(c) liquid and (d)–(f) ice condensates and grid-mean (g)–(i) liquid and (j)–(l) ice condensates. In (a)–(f), white color denotes the area without corresponding clouds.
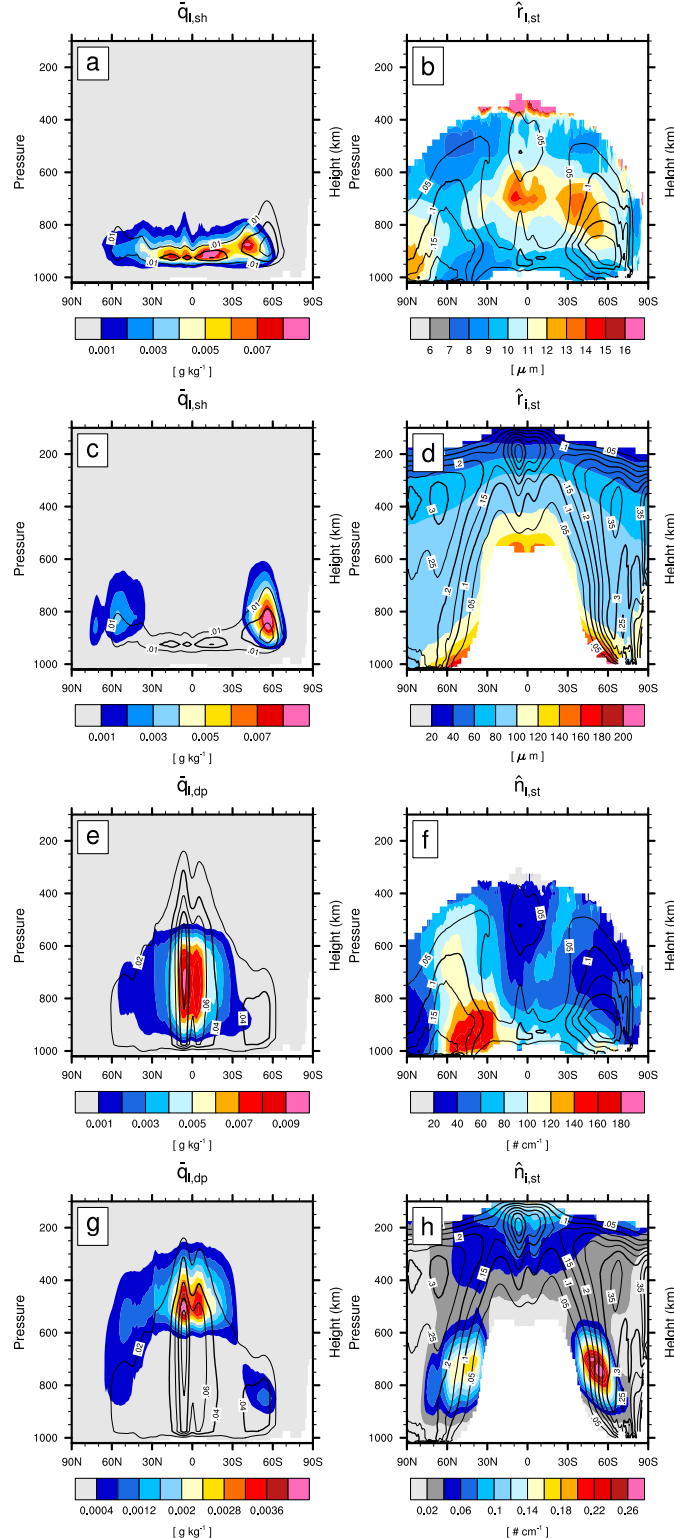
FIG. 10. CAM5-simulated annual zonal-mean cross sections of (left) grid-mean LWC and IWC from shallow and deep cumulus (color shading) and (right) effective radius and number concentrations of stratus liquid droplets and ice crystals (color shading). In each plot, cloud fraction— (a),(c) A_{sh}; (e),(g) A_{dp}; (b),(f) $A_{l,st}$; and (d),(h) $A_{i,st}$— is overlaid as solid lines. In (right), white color denotes the area without corresponding clouds.

the tropics, where $\overline{q}_{l,\text{st}}$ in the maritime continents is very high and additional stratocumulus decks exist over the SST warm frontal region to the north of the SST cold tongue in the eastern equatorial Pacific Ocean (Fig. 8g). In the midlatitudes, nonzero $\overline{q}_{l,\text{st}}$ extends down to the surface especially during JJA in the Northern Hemisphere (NH), indicating the existence of advection fog (see Fig. 11d).

As expected from Eq. (3), the pattern of $A_{l,\text{st}}$ (Fig. 10b) is similar to the pattern of grid-mean RH (not shown), but the pattern of $A_{i,\text{st}}$ (Fig. 10d) more closely resembles $\overline{q}_{i,\text{st}}$ than the grid-mean RH [Fig. 9k and Eq. (4)]. Near the surface in the Arctic, $A_{i,\text{st}}$ during DJF ($A_{l,\text{st}}$ during JJA) reaches up to 0.6 (0.35) but the corresponding $\hat{q}_{i,\text{st}}$ is very small (Figs. 9b,e).

In the entire globe, $\hat{r}_{i,\text{st}}$ is much larger than $\hat{r}_{l,\text{st}}$. While $\hat{r}_{i,\text{st}}$ decreases with the height and the latitude, $\hat{r}_{l,\text{st}}$ shows maxima in the midtroposphere and over the Arctic. The Northern Hemispheric $\hat{n}_{l,\text{st}}$ is much larger than that in the Southern Hemisphere, with maximum values over $160\,\text{cm}^{-3}$ in the subtropical and midlatitude lower troposphere extending up to the midtroposphere, which is roughly similar to the satellite estimates (Bennartz 2007). This demonstrates the indirect effects of continental and anthropogenic aerosols emitted from industrialized areas, which are propagated downstream and poleward and upward in height by the midlatitude westerly jet and synoptic storm track. On the other hand, CAM5 simulates maximum $\hat{n}_{i,\text{st}}$ in the tropical upper troposphere ($0.1\,\text{cm}^{-3}$) and in the midlatitude regions at $\sim700\,\text{hPa}$ during boreal winter (0.2–$0.3\,\text{cm}^{-3}$), where shallow cumulus detrains its LWC (IWC) with a specified effective volume radius of 10 (50) μm (see Fig. 10c). The interhemispheric contrast of $\hat{n}_{i,\text{st}}$ is much weaker than $\hat{n}_{l,\text{st}}$.

From the above analysis, the CAM5-simulated cloud systems can be grouped into the following six categories: 1) deep cumulus mainly in the tropics; 2) shallow cumulus between the tropics/subtropics and the midlatitude regions; 3) thick stratus in the midlatitude storm track throughout the whole troposphere, especially during boreal winter; 4) cirrus in the tropical–extratropical upper troposphere; 5) marine stratocumulus over the midlatitude oceans, eastern subtropical oceans on the west of the major continents, and the northern flank of the SST front in the eastern equatorial Pacific Ocean; and 6) optically thin Arctic low-level clouds. These cloud features are in fact quite similar to what is observed in nature.

g. PBL top height, fog, and low-cloud amount

Figure 11 shows CESM1 and CCSM4-simulated PBL top heights and the amount of fog during JJA. Low-cloud amount (LCA) is plotted as solid lines on the left panel of Fig. 12. CAM5/CAM4 produced similar results as the ones from CESM1/CCSM4 (not shown). In the subtropical stratocumulus decks west of the major continents, CESM1 simulates a much deeper PBL than CCSM4. This deepening feature extends westward into the midlatitude oceans including the 60°S latitude band and also into the SST frontal region over the eastern equatorial Pacific Ocean, although it is offset by other factors that force CESM1 to simulate a shallower PBL than the CCSM4 (e.g., in contrast to CAM3/CAM4, CAM5 uses turbulent mountain stress that may decrease surface wind speed and the PBL top height; as detailed in the caption of Fig. 11, in defining PBL top height, 1) CAM4 uses 0.3 while CAM5 uses the more strict value of 0.19 for the critical Richardson number; 2) CAM4 imposes a certain minimum PBL top height while CAM5 does not; and 3) in cases of decoupling, the CAM5 PBL top height is defined as the top interface of surface-based convective layers). The deeper PBL in CESM1 over the marine stratocumulus deck is partly due to strong cloud-top entrainment driven by cloud-top radiative cooling that is explicitly incorporated into the computation of buoyancy production at the PBL top. Strong entrainment at the PBL top dries the PBL by bringing warmer and drier free air into the PBL.

The drier air in the lower PBL in CESM1 is clearly reflected in the simulated fog amount in Fig. 11. During JJA, observations show the maximum fog amount on the northwestern flank of the subtropical high where warm and moist air is advected over the cold ocean across the SST front, forming advection fog. CCSM4 roughly captures the spatial distribution of observed fog but the magnitude is much larger than the observations, with anomalous fog over the subtropical stratocumulus decks west of the major continents, over the southwestern Arabian Sea and over the SST cold tongue along the equator in the eastern equatorial Pacific Ocean. CESM1 does a much better job: the fog amount over the northwestern flank of the subtropical high is smaller than in CCSM4, and anomalous fog over the subtropical stratocumulus decks and western Arabian Sea has completely disappeared, with better simulation along the SST cold tongue. This improvement in CESM1 is due to enhanced turbulent mixing and drying of the lower PBL, as a result of the simulation of cloud–radiation–turbulence interactions in CAM5.

Over some portions of the Antarctic sea ice area during JJA (e.g., at around 180° and 50°W along 75°S), however, CESM1 simulates more fog than CCSM4. We speculate that the changes of the horizontal advection, synoptic storm activity, and surface wind speed may be responsible for this increase of fog from CCSM4 to CESM1 during boreal winter.
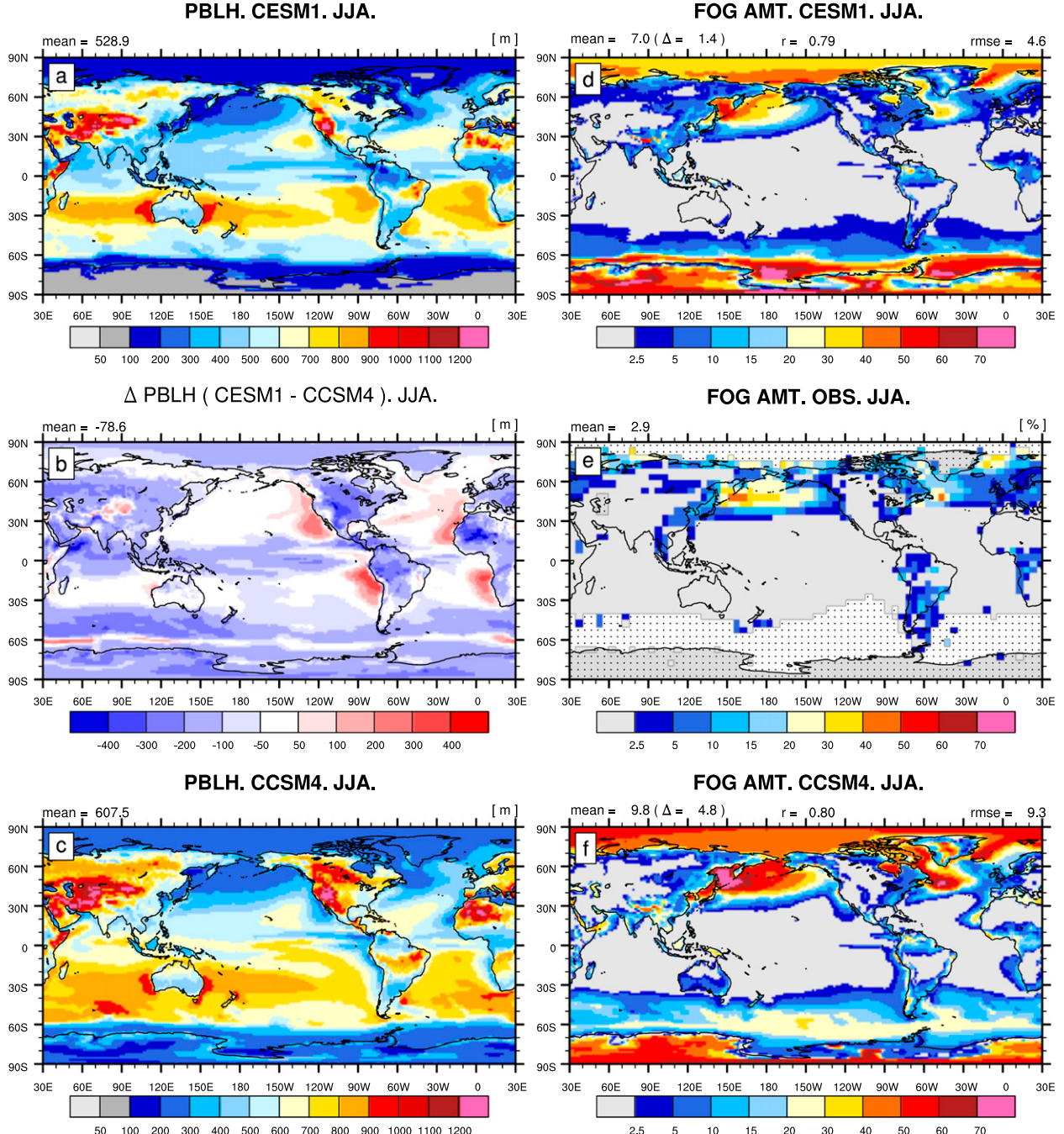
FIG. 11. (left) Diagnostic PBLH in JJA from (top) CESM1, (bottom) CCSM4, and (middle) CESM1 minus CCSM4. (right) Fog amount in JJA from (top) CESM1, (bottom) CCSM4, and (middle) EECRA observations. Simulated fog amount is defined as A_{tot} in the lowest model layer located at $z = 67$ m over the ocean. Observed fog amount is defined as total cloud fraction when surface observer reported fog [ww = 10–12 and 40–49 where ww is a present weather code defined from WMO (1975)]. In CAM4, PBLH is defined as the lowest interpolated height, where the dry bulk Richardson number computed upward from the lowest model layer is larger than 0.3, with additional adjustment if surface buoyancy flux (B_s) is positive. A minimum value of $700 \times u_*$ meters (u_* is surface frictional velocity) is imposed on the diagnosed PBLH. In CAM5, if $B_s < 0$ ($B_s > 0$), PBLH is defined as z_H, the layer midpoint height just below the lowest model interface (as the height of the lowest model interface) where the moist gradient Richardson number is >0.19. When $B_s > 0$, PBLH is allowed to rise into the next model interface as detailed in Bretherton and Park (2009). No minimum value is imposed on the diagnosed PBLH in CAM5 but by construction PBLH is always larger than the midpoint height of the lowest model layer.

h. *Lower-tropospheric stability versus LCA*

Because of the explicit parameterization of cloud–radiation–turbulence interaction, CESM1 does not need a separate parameterization for stability-based stratus fraction. However, if the simulated cloud–radiation–turbulence interactions are realistic, CESM1 should be able to reproduce the observed relationship between lower-tropospheric stability (LTS; LTS $\equiv \theta_{700hPa} - \theta_{1000hPa}$) and stratus fraction (Klein and Hartmann 1993) that was built into CCSM4.

Figure 12 shows the interannual correlation coefficient between LTS and LCA from the observations, CESM1, and CCSM4 during JJA. For comparison, climatological LCA from the observations and individual simulations is also plotted as solid lines in each figure. Observations show a maximum in LCA over the subtropical stratocumulus decks west of the major continents, midlatitude oceans, SST front in the eastern equatorial Pacific Ocean, and the Arctic. CCSM4 captures the observed maxima of LCA partly with the help of the stability-based stratus fraction. Even without the stability-based stratus, however, CESM1 successfully simulates the observed LCA maxima over the aforementioned areas, including the local minimum LCA along the equator slightly north of the SST cold tongue in the eastern equatorial Pacific Ocean.

Observations also show significant positive correlation between LTS and LCA over the subtropical stratocumulus decks, over midlatitude oceans in the NH, and in the vicinity of the SST cold tongue in the eastern equatorial Pacific Ocean. By construction, CCSM4 simulates a strong positive correlation between LTS and LCA. Without stability-based stratus, CESM1 successfully captures the observed significant positive correlations. This figure demonstrates that the cloud–radiation–turbulence interactions simulated in CESM1 realistically reproduce complex feedback processes that control the observed positive relationship between LTS and LCA over the marine stratocumulus decks. However, simulated positive correlations are generally stronger and more ubiquitous than the observations, especially over the tropics and the major continents. This implies possible model deficiencies, although sampling noise in the relatively sparse observations may contribute to this difference. Both CCSM4 and CESM1 simulate significant negative correlations over the Arctic and Antarctic, with stronger negative correlation in CESM1 over the Arctic in summer.

i. *Radiative feedback of marine stratocumulus at the surface*

Marine stratocumulus (MSC) reflects incoming solar radiation and cools the underlying sea surface. In turn,

cold SST favors the formation of MSC by increasing the degree of vertical coupling of thermodynamic variables within the PBL. During the tuning process of CAM5–CESM1, we found that a version of CAM5 with excessive SW CRF over the North Pacific Ocean would drift toward very cold SSTs after dynamical ocean coupling, even though fixed SST simulations produced a good global energy balance at TOA. This drift in the coupled system was eventually solved by retuning CAM5 to produce closer agreement with the observed SW CRF over the North Pacific Ocean. Correct simulation of future climate critically depends on how the model accurately simulates the positive feedback between SST and MSC (Bodas-Salcedo et al. 2012; Williams et al. 2013).

Park et al. (2005) quantitatively estimated the strength of this positive MSC–SST feedback by computing surface heat flux feedback (i.e., the response of surface heat flux to sea surface temperature anomalies) using the observed monthly SST and the surface radiative flux dataset. They showed that positive MSC–SST feedback is strong along the SST gradient zone over the subtropical and midlatitude oceans where the transition between stratocumulus and cumulus occurs. Using a stochastically forced ocean mixed layer model, Park et al. (2006) also showed that positive MSC–SST feedback can substantially enhance the persistence of SST anomalies during late spring and early summer over the North Pacific Ocean.

The right panels of Fig. 12 show surface SW radiative feedback during JJA estimated following the methodology of Park et al. (2005) to produce observed and model estimates. With a change in sign, the surface SW radiative feedback measures how much net downwelling SW radiation at the surface changes when the underlying SST increases by 1 K. Observations show strong positive SW feedback along the SST gradient zone in the midlatitudes and eastern subtropical Pacific Ocean in association with the transition of stratocumulus to cumulus when the underlying SST increases. The maximum magnitude of SW radiative feedback at the surface amounts to $40 \, \mathrm{W \, m^{-2} \, K^{-1}}$ over the northwestern flank of the Namibian stratocumulus deck during September–November (SON; not shown). Both CCSM4 and CESM1 reproduce the observed SW radiative feedback. The success of CCSM4, mainly due to the empirical parameterization for stability-based stratus fraction, is somewhat surprising since CAM3/CAM4 do not generate in-cloud condensate within the stability-based stratus. Without the stability-based stratus, CESM1 successfully reproduces the observed positive MSC–SST feedback at the right location and magnitude, because of the explicit parameterization of cloud–radiation–turbulence interactions. Strong positive feedback over the summer Arctic, both in CESM1 and CCSM4, reflects the melting of sea ice
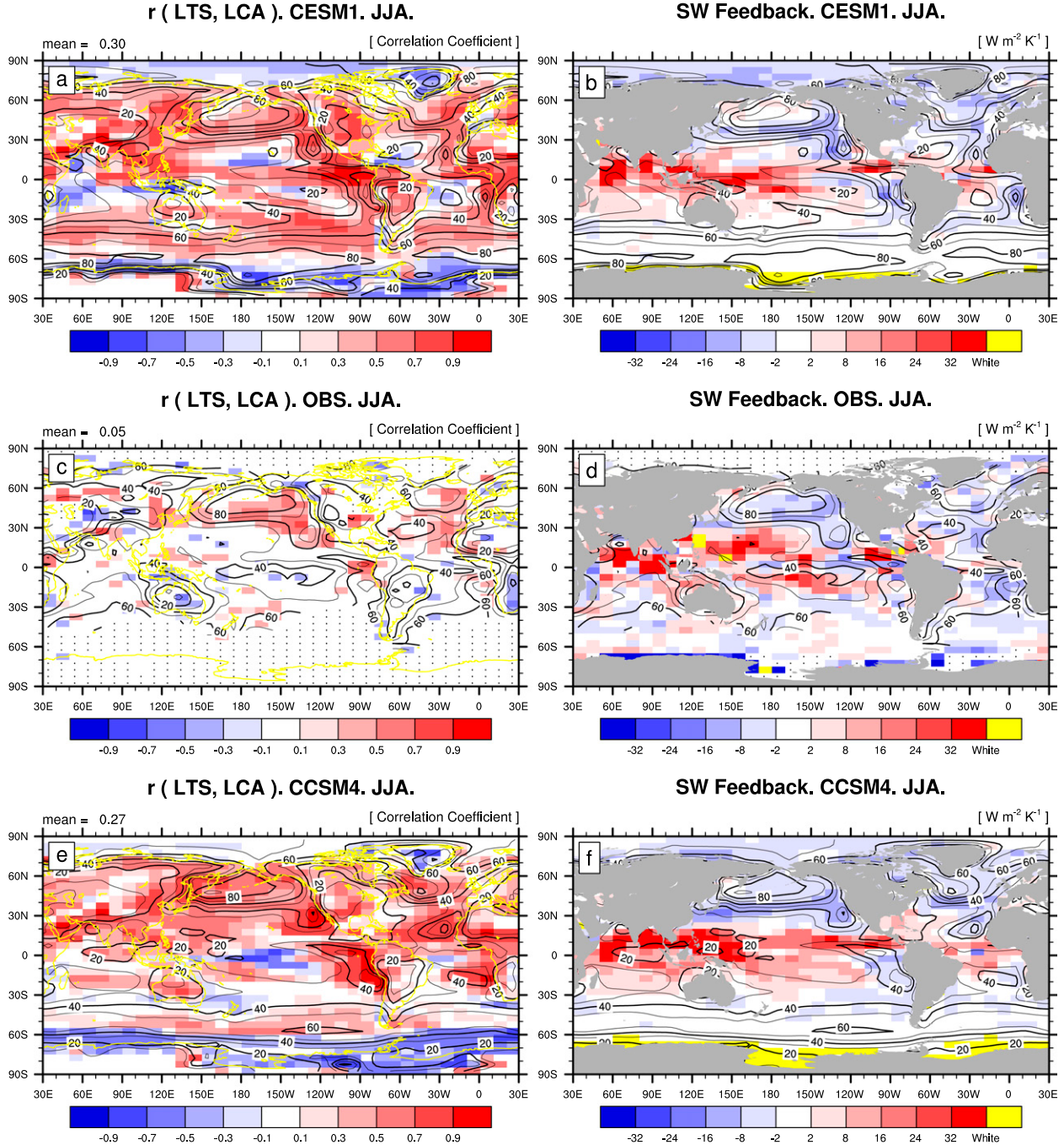
FIG. 12. (left) Interannual correlation coefficient (r) between LTS ($\theta_{700hPa} - \theta_{1000hPa}$) and LCA. (right) Surface heat flux feedback parameter for SW radiation (λ_{SW}) computed from (top) CESM1, (middle) observations, and (bottom) CCSM4 in JJA. Climatological LCA during JJA is overlaid as solid lines in each plot. Simulated r is computed using 156 yr (January 1850–December 2005) of detrended monthly output from twentieth-century coupled simulations while observed LCA and LTS are from the detrended 53 (ocean) and 26 yr (land) of EECRA surface observations and detrended National Centers for Environmental Prediction–National Center for Atmospheric Research (NCEP–NCAR) reanalysis product (Kalnay et al. 1996), respectively. Only the grid boxes with statistically significant r at the 95% confidence level from the two-sided t test (assuming independent samples) are shaded either by red or blue colors. The λ_{SW} is estimated using the lagged covariance between monthly SST anomalies and net upwelling SW radiative flux anomalies at the surface, following Park et al. (2005). Physically, negative (positive) λ_{SW} indicates the increase (decrease) of net downwelling SW radiative flux at the surface when underlying SST increases by 1 K, implying positive (negative) feedback between the surface temperature and net downwelling SW radiative flux at the surface. The grid boxes with yellow shading denote the area with statistically nonsignificant monthly persistency of underlying surface temperature, so no feedback estimation is performed there.

and the decrease of clear-sky surface albedo in association with the increase of surface temperature, rather than the effects of clouds which are optically thin there.

j. Sensitivity of the cloud system to key uncertain parameters

This section provides insight into the sensitivity of CAM5-simulated clouds to several key parameters that were optimized during the tuning process, rather than being strictly constrained against observations. Figures 13 and 14 show the changes of SW CRF at TOA (color in Fig. 13), LW CRF at TOA (line in Fig. 13), condensate water path (CWP; CWP = TGCLDLWP + TGCLDIWP; color in Fig. 14), and CLDTOT (line in Fig. 14) from the control simulation when individual parameter values are perturbed from the CAM5 default value as indicated at the top of each figure. The physical meaning of each of the eight parameters is as follows: a_{2l} is the evaporative enhancement factor of entrainment rate at the top of cloud-topped convective layers (Fig. 13a); r_{pen} is the penetrative entrainment efficiency at the top of shallow convective updraft (Fig. 13b); c_o is the autoconversion efficiency of deep convective condensate into precipitation (Fig. 13c); $q_{i,st,min}$ is the minimum in-stratus IWC that stratus can hold (Fig. 13d); $R_{det,dp}$ is the effective radius of detrained deep convective condensate (Fig. 13e); $R_{det,sh}$ is the effective radius of detrained shallow convective condensate (Fig. 13f); $D_{c,s}$ is the critical diameter of ice crystals at which stratus ice condensate starts to be converted into snow (Fig. 13g); and $w_{ice,max}$ is the maximum subgrid vertical velocity for the activation of stratus ice nuclei (Fig. 13h).

If a_{2l} is reduced, the top-of-stratocumulus-topped PBL becomes moister because of the reduction of entrainment warming and drying, resulting in increases of LCA, TGCLDLWP, and SW CRF cooling over the subtropical and midlatitude stratocumulus decks over the ocean (Figs. 13a and 14a). The parameter r_{pen} has a similar effect to a_{2l} except that the effect of r_{pen} is stronger in the downstream portion of the subtropical stratocumulus deck in which shallow cumulus lies underneath stratocumulus (Figs. 13b and 14b). The negative regional biases of SW CRF (Fig. 3e), CLDTOT (Fig. 4e), and TGCLDLWP (Fig. 4f) in the eastern subtropical ocean west of the major continents can be adjusted by reducing a_{2l} and r_{pen}.

If the production rate of deep convective precipitation decreases because of the decrease of c_0, deep convective updrafts can hold more in-cumulus condensate: some of which is detrained and forms the stratiform condensate in the tropics, which in turn is transported into the extratropical regions by the Hadley

circulation and resolved eddy motions, resulting in substantial increases of CWP, SW CRF cooling, and LW CRF warming, in both the tropical and extratropical regions (Figs. 13c and 14c). Some of the negative biases of TGCLDLWP (Fig. 4f) can be offset by reducing c_0, but the negative bias of SW CRF (Fig. 3e) in the tropical deep convection regime will be degraded. If $q_{i,st,min}$ increases, CAM5 decreases the fractional amount of optically thin ice stratus without changing the grid-mean IWC of stratus. The largest decrease in ice stratus fraction can be seen in the tropical upper troposphere and polar regions, without much change to CWP and CRFs (Fig. 14d). The positive biases of CLDTOT in the polar regions (Fig. 4e) can be offset by increasing $q_{i,st,min}$.

The CAM5 cloud system is surprisingly insensitive to the specified sizes of detrained deep convective condensates. Deep convective condensate is detrained mostly in the tropics (Figs. 8c,d and 10e,g), where convective precipitation is dominant over stratiform precipitation (Figs. 6a,b). In addition, in-cloud LWC/IWC of deep cumulus in CAM5 is very low because of the use of a very large autoconversion efficiency (Figs. 9a,d). Thus, the change in $R_{det,dp}$ does not have much impact on the hydrological cycle, CWP (Fig. 14e), and CRFs (Fig. 13e). In contrast to deep convection, the size of detrained shallow convective condensate has a large influence on the midlatitude cloud system. Detrained shallow convective IWC serves as an important source of ice stratus IWC in the midlatitudes (Figs. 10c,h), where stratiform precipitation is dominant over convective precipitation (Figs. 6a,b). As a result, small $R_{det,sh}$ decreases stratiform precipitation, resulting in an increase of CWP and SW CRF cooling in the midlatitude storm track. This change would reduce the SWCF bias in the SH storm track. In fact, smaller $R_{det,sh}$ is more comparable with the satellite estimates (King et al. 2013).

If $D_{c,s}$ decreases, more in-stratus IWC can be converted into snow, resulting in a decrease of TGCLDIWP and the associated ice stratus fraction (Fig. 14g). In the tropics, both SW and LW CRFs become consistently weaker, but SW CRF cooling increases in the midlatitude storm track, even though CWP decreases there (Fig. 13g). This is partly due to the increase of diagnostic snow amount and its radiative impact: CAM5 explicitly includes the SW radiative effect of snow. If $w_{ice,max}$ decreases, the nucleation rate of aerosols into cloud ice droplet decreases [at $z = 200$-hPa height in the tropical deep convection region, the frequency of $w_{ice} \geq w_{ice,max} = 0.2 \, \text{m s}^{-1}$ (so that w_{ice} is reset to $w_{ice,max}$ for the aerosol nucleation) is about 0.15–0.3 (not shown)], resulting in a decrease of ice stratus fraction, SW CRF cooling, and LW CRF warming, mostly in the tropical deep convection regimes (Figs. 13h and 14h).
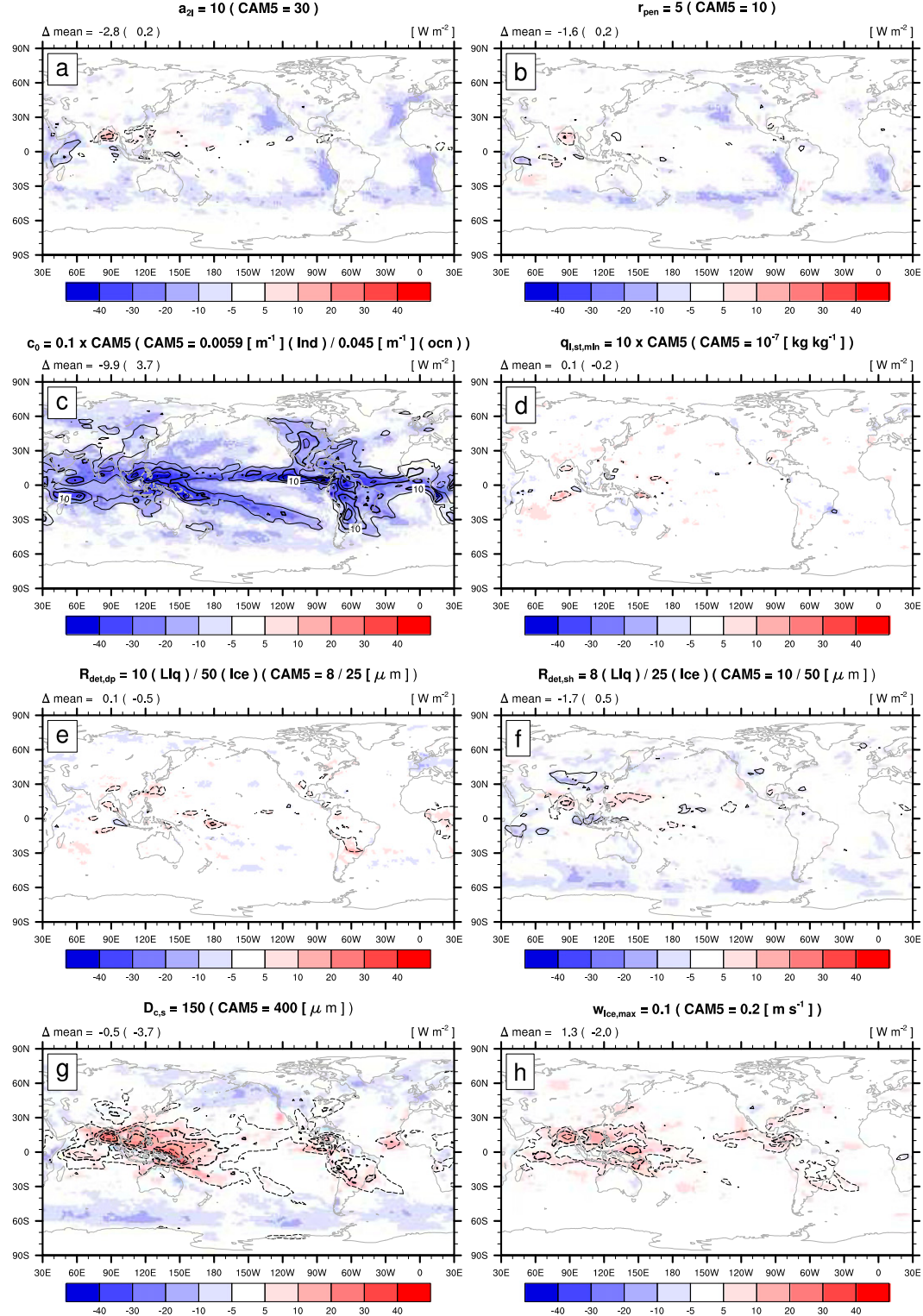
FIG. 13. Sensitivity of CAM5 cloud system to several uncertain model parameters. The plots show the changes of SW CRF (color shading) and LW CRF (solid–dashed black lines, where the dashed line is for a negative value) at TOA, when the individual parameter is perturbed from the default value as denoted at the top of each plot. The values at the top left of individual plots are the global-mean values of ΔSW CRF (ΔLW CRF). Contour interval is 5 W m^{-2}. See the text for the physical meaning of the perturbed parameters.

4. Summary and conclusions

This paper provides a description of the integrated representation for cloud processes in CAM5. Compared with the previous versions, the cloud parameterizations in CAM5 are more consistent and physically based, due to inclusion of more realistic and complex parameterizations and much attention given to the interactions among them within a more consistent framework. Several key aspects of CAM5 cloud parameterizations are 1) a consistent cloud macrophysical formulation, 2) stratus–radiation–turbulence interactions, 3) prognostic treatment of stratus droplet number and aerosol species, and 4) radiatively active cumulus and snow.

Within each grid layer, CAM5 has nonoverlapped deep cumulus, shallow cumulus, and stratus, where each of which has its own cloud fraction, in-cloud mass, and number concentration of cloud droplets. Deep and shallow convection schemes diagnose vertical profiles of cumulus properties. Liquid and ice stratus fractions are diagnosed as a function of grid-mean RH over water and ice, respectively, and a single stratus fraction is diagnosed by assuming maximum horizontal overlap between the two. The saturation equilibrium constraint (i.e., RH over water within liquid stratus is 1, and liquid stratus condensate does not exist outside of liquid stratus) allows CAM5 to compute the net condensation rate of water vapor into liquid stratus. By performing pseudo condensation–evaporation (adjusting the ice stratus fraction), consistency is imposed between the diagnosed cloud fraction and the prognosed condensate amount of liquid (ice) stratus at the end of stratus macrophysics, which removes empty (i.e., zero in-stratus condensate) and dense (i.e., very large in-stratus condensate) stratus. On the other hand, CAM4 allows horizontal overlap without occupancy priority among the three clouds, only diagnoses a single-phase stratus fraction, uses stability-based empty stratus as well as RH-based stratus, and frequently generates empty and dense stratus.

The CAM5 moist turbulence scheme handles both the dry and saturated turbulent processes throughout the whole atmosphere, while the CAM4 PBL scheme handles only dry turbulent processes within the PBL. By incorporating cloud-top LW cooling into the computation of eddy diffusivity, CAM5 explicitly simulates stratus–radiation–turbulence interactions that can sustain a saturated PBL top over the ocean by enhancing turbulent vertical mixing. As a result, CAM5 simulates marine stratocumulus (MSC) at the PBL top solely from the grid-mean RH without relying on separate empirical stability-based prescription of stratus cloud fraction. With stratus–radiation–turbulence interaction, MSC is a dynamic driver of the climate system as well as the controller of the global radiation budget and hydrological cycle. Parameterization of stratus–radiation–turbulence interaction imposes direct interaction among stratiform macrophysics, radiation, and moist turbulence schemes (Fig. 1) that are absent in CAM4.

As well as the mass, CAM5 prognoses number concentration of stratus droplets. The two main sources of stratus droplet numbers are activated aerosols and detrained in-cumulus condensates, while the main sinks are evaporation, sedimentation, and precipitation of stratus condensates. Both deep and shallow convection schemes only diagnose the mass of in-cumulus condensate. CAM5 specifies the mean volume radius of detrained in-cumulus condensate and derives condensate number from the condensate mass and size. Through the activation process, aerosol controls the stratus droplet size, which affects the radiation and the production rate of stratiform precipitation. In other words, CAM5 simulates various aerosol indirect effects associated with stratus. Since aerosol activation occurs when subsaturated turbulent eddies are delivered into the saturated stratus portion, direct interaction among stratiform macrophysics, aerosol activation, and moist turbulence schemes are included in the CAM5 processes (Fig. 1). Grid-scale advection and moist PBL schemes transport stratus droplets, assuming that they are conserved during transport. Instead of prognosing droplet number concentration, CAM4 specifies a fixed radius of stratus droplets over land and ocean with a ramp between them.

CAM5 explicitly handles the radiative effects of cumulus and snow by assuming that in-cumulus condensate (not the detrained condensate) has the same droplet radius and size distribution parameters as the in-stratus condensate in the same layer. However, internal thermodynamic properties of cumulus are not advected by the large-scale advection scheme.

In addition to the more comprehensive and consistent model physics, CAM5–CESM1 has improved climate fidelity. However, several systematic biases were also identified in the simulated cloud fields in CAM5. Through a set of parameter sensitivity simulations and a detailed review of model parameterizations, we could identify (or speculate on) the source of the discrepancies down to the process level, which can be grouped into the following three categories: 1) deficient regional tuning, 2) inconsistency between various physics parameterizations, and 3) incomplete model physics.

Parameter sensitivity simulations provided potential pathways to address the following biases:

- negative biases of CLDTOT and associated CRFs in the eastern subtropical oceans can be reduced by reducing penetrative entrainment efficiency at the shallow cumulus top;
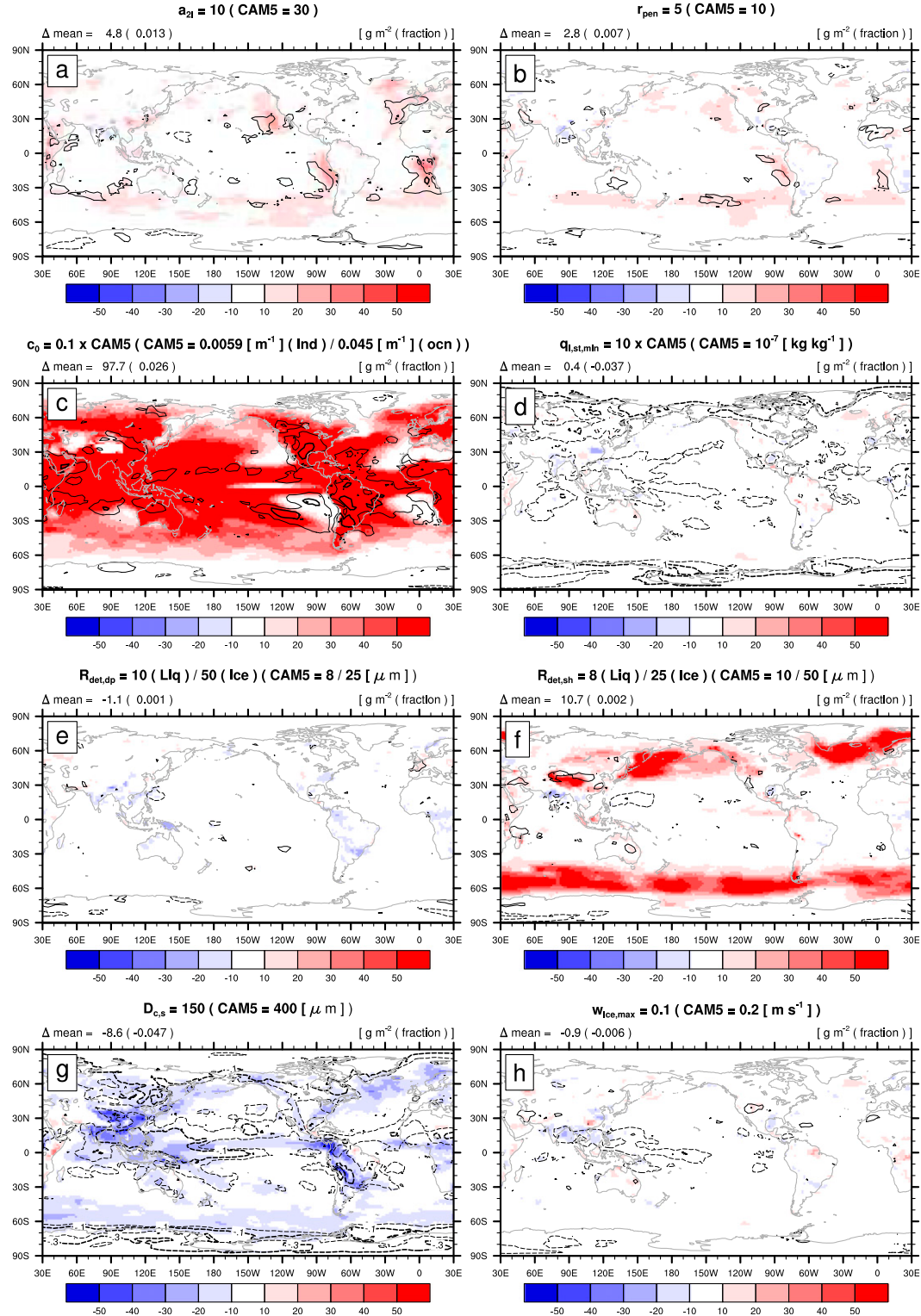
FIG. 14. As in Fig. 13, but the changes of CWP (color shading) and TCA (solid–dashed black lines, where a dashed line is for negative values). The values at the top left of individual plots are the global-mean values of ΔCWP (ΔTCA). Contour interval is 0.05 for the first contour and 0.1 for the other contours.

- positive biases of CLDTOT over polar regions can be reduced by increasing minimum in-stratus IWC thresholds;
- negative biases of TGCLDLWP can be partially addressed by reducing autoconversion efficiency of deep cumulus condensate or by reducing the effective radius of detrained shallow cumulus condensate;
- weak SW CRF over the SH storm track can be reduced by decreasing the effective radius of detrained shallow cumulus condensate;
- some of the overly strong SW CRF and LW CRF in the tropics can be addressed by reducing the deep cumulus fraction; and
- too frequent deep convective activity might be addressed by reducing the CAPE consumption time scale.

One example of the inconsistency between different parameterizations is the aerosol activation performed in the middle of stratiform microphysics rather than at the beginning, resulting in overestimation of stratus droplet size used for the computation of stratiform precipitation production and the negative bias of TGCLDLWP.

The biases possibly associated with incomplete model physics are as follows:

- underestimation of LW CRF due to the horizontal heterogeneity assumption of water vapor within each grid layer in the radiation scheme;
- overly strong SW CRF and LW CRF in the tropics due to the use of a single-type cloud within the radiation scheme; and
- underfrequent shallow convective activity over summer continents due to the neglect of forced convection.

In summary, CAM5 provides the community with a unique opportunity to explore cloud–aerosol–climate interactions in a physically reasonable way. While substantially improved from its predecessors, many aspects of CAM5 can and should be improved in the future, upon which we are continuously working with collaborators.

APPENDIX A

Cloud Macrophysics for Liquid Stratus

This section provides information on the CAM5 cloud macrophysics for liquid stratus. Cloud macrophysics is
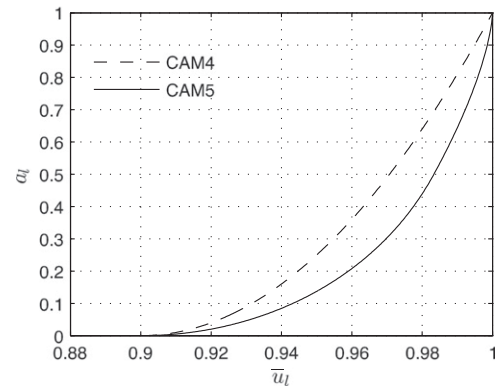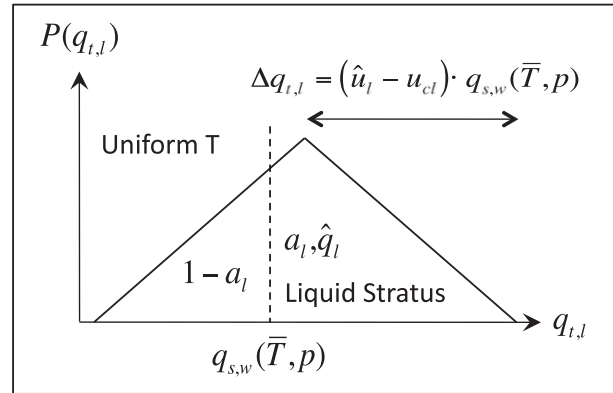
FIG. A1. (top) Triangular PDF of total liquid specific humidity ($q_{t,l}$) used for computing liquid stratus fraction (a_l) in CAM5. Liquid stratus fraction is the area on the rhs of the dashed line of $q_{t,l} = q_{s,w}$ where $q_{s,w}$ is saturation specific humidity over water. In principle, in-stratus LWC ($\hat{q}_l$), as well as a_l, can be diagnosed but CAM5 only uses a_l from the triangular PDF. The half-width of triangular PDF is directly related to the critical relative humidity u_{cl} that is used as a tuning parameter, rather than being internally computed as discussed in the main text. (bottom) The a_l as a function of grid-mean relative humidity over water ($\overline{u}_l$) from both CAM4 and CAM5 when $u_{cl} = 0.9$.

a set of physical processes used to compute cloud fraction and net condensation rate of water vapor into cloud water. On the other hand, cloud microphysics is a set of processes used to generate precipitation from cloud water. We will explain how CAM5 computes diagnostic liquid stratus fraction ($a_{l,st}$) and prognostic grid-mean net condensation rate of water vapor into liquid stratus water ($\overline{Q}_l$). Then, we will explain how CAM5 imposes consistency between diagnostic stratus fraction and prognostic stratus water within the process-splitting framework.

a. Liquid stratus fraction

To compute liquid stratus fraction (a_l), following Smith (1990), we assume that the area PDF (P) of total liquid specific humidity ($q_{t,l} \equiv q_v + q_l$ defined without q_i) follows a triangular distribution but temperature is

uniform [i.e., T follows a δ function with $P(T) = \infty$ at $T = \overline{T}$ while $P(T) = 0$ at $T \neq \overline{T}$] within each grid layer (see Fig. A1). For simple notation, we will use $a_l \equiv a_{l,\text{st}}$ and $q_l \equiv q_{l,\text{st}}$ in this section. Mathematically, this triangular PDF can be represented by the following normalized area PDF:

$$P(z) = 1 - |z|, \quad -1 \leq z \equiv \left(\frac{v_l - v_{l,m}}{\Delta v_l}\right) \leq 1, \quad \text{(A1)}$$

where $v_l \equiv q_{t,l}/q_{s,w}(\overline{T}, p)$ is total liquid RH, $v_{l,m}$ is v_l at the midpoint ($z = 0$) of the distribution (or equivalently $v_{l,m}$ is identical to the grid-mean v_l, $v_{l,m} = \overline{q}_{t,l}/q_{s,w}(\overline{T}, p)$, since triangular PDF is symmetric), and Δv_l is the half-width of v_l in the distribution. The variance of z is $1/6$, $\overline{q}_{t,l} = v_{l,m}q_s(\overline{T}, p)$ and the half-width of $q_{t,l}$ is $\Delta q_{t,l} = \Delta v_l q_s(\overline{T}, p)$. If we know $(\overline{T}, \overline{q}_{t,l}, \Delta q_{t,l})$ in each layer, we can compute $a_l = \int_{z_s}^{1} P(z)\,dz$, where $z_s \equiv (1 - v_{l,m})/\Delta v_l$, $\hat{q}_l = (1/a_l)q_s(\overline{T}, p)\int_{z_s}^{1}(v_{l,m} + \Delta v_l z - 1)P(z)\,dz$, and grid-mean relative humidity over water $\overline{u}_l \equiv \overline{q}_v/q_{s,w}(\overline{T}, p) = \int_{-1}^{z_s}(v_{l,m} + \Delta v_l z)P(z)\,dz + \int_{z_s}^{1}P(z)\,dz$. Through algebraic computations, we can derive

$$a_l = \begin{cases} 1, & \hat{x} < -1 \\ 1 - (1/2)(1+\hat{x})^2, & -1 \leq \hat{x} < 0 \\ (1/2)(1-\hat{x})^2, & 0 \leq \hat{x} < 1 \\ 0, & 1 \leq \hat{x} \end{cases}; \quad \text{(A2)}$$

$$\left[\frac{\hat{q}_l}{q_{s,w}(\overline{T}, p)}\right]\left(\frac{1}{\Delta v_l}\right)$$

$$= \begin{cases} -\hat{x}, & \hat{x} < -1 \\ a_l^{-1}[(1/6) - (\hat{x}^2/2)[1 + (2/3)\hat{x}]] - \hat{x}, & -1 \leq \hat{x} < 0 \\ a_l^{-1}[(1/6) - (\hat{x}^2/2)[1 - (2/3)\hat{x}]] - \hat{x}, & 0 \leq \hat{x} < 1 \\ 0, & 1 \leq \hat{x} \end{cases};$$

and

(A3)

$$\left(\frac{\overline{u}_l - \hat{u}_l}{\Delta v_l}\right) = \begin{cases} 0, & \hat{x} < -1 \\ -(1/6)(1+\hat{x})^3, & -1 \leq \hat{x} < 0 \\ -\hat{x} - (1/6)(1-\hat{x})^3, & 0 \leq \hat{x} < 1 \\ -\hat{x}, & 1 \leq \hat{x} \end{cases}, \quad \text{(A4)}$$

where

$$\hat{x} \equiv \left(\frac{\hat{u}_l - v_{l,m}}{\Delta v_l}\right) \quad \text{(A5)}$$

and $\hat{u}_l = 1$ is in-stratus RH. Equation (A2) computes a_l as a combined quadratic function of $\overline{v}_l = (\overline{q}_v + \overline{q}_l)/q_{s,w}(\overline{T}, p)$. We can also represent $\hat{q}_l$ and $\overline{u}_l$ as a function of a_l as

$$\left[\frac{\hat{q}_l}{q_s(\overline{T}, p)}\right]\left(\frac{1}{\Delta v_l}\right)$$

$$= \begin{cases} \left(\frac{\sqrt{2}}{3}\right)a_l^{1/2}, & 0 \leq a_l < 0.5 \\ a_l^{-1}\left[1 - \left(\frac{\sqrt{2}}{3}\right)(2 + a_l)(1 - a_l)^{1/2}\right], & 0.5 \leq a_l \leq 1 \end{cases}$$

and

(A6)

$$\left(\frac{\overline{u}_l - \hat{u}_l}{\Delta v_l}\right) = \begin{cases} -1 + \left(\frac{\sqrt{2}}{3}\right)a_l^{1/2}(3 - a_l), & 0 \leq a_l < 0.5 \\ -\left(\frac{\sqrt{2}}{3}\right)(1 - a_l)^{3/2}, & 0.5 \leq a_l \leq 1 \end{cases}. \quad \text{(A7)}$$

By reverting Eq. (A7), a_l can be written as a function of $\overline{u}_l$ as follows:

$$a_l = \begin{cases} 1, & \hat{u}_l \leq \overline{u} \\ 1 - \left[\frac{3}{\sqrt{2}}\left(\frac{\hat{u}_l - \overline{u}_l}{\Delta v_l}\right)\right]^{2/3}, & \hat{u}_l - \frac{\Delta v_l}{6} \leq \overline{u}_l < \hat{u}_l \\ 4\left[\cos\left(\frac{1}{3}\left\langle\arccos\left\{\frac{3}{2\sqrt{2}}\left[1 - \left(\frac{\hat{u}_l - \overline{u}_l}{\Delta v_l}\right)\right]\right\} - 2\pi\right\rangle\right)\right]^2, & \hat{u}_l - \Delta v_l \leq \overline{u}_l < \hat{u}_l - \frac{\Delta v_l}{6} \\ 0, & \overline{u}_l \leq \hat{u}_l - \Delta v_l \end{cases}. \quad \text{(A8)}$$

By using critical RH for liquid stratus defined as $u_{cl} \equiv \hat{u}_l - \Delta v_l$, the above equation can be written as Eq. (3). Liquid stratus fraction can be formed only when $\overline{u}_l \geq u_{cl}$ and the large value of u_{cl} implies a narrow PDF. Figure A1 shows plots of $a_l(\overline{u}_l)$ from Eq. (A8) used in CAM5 and from the quadratic formula $\{a_l(\overline{u}_l) = [(\overline{u}_l - u_{cl})/(1 - u_{cl})]^2\}$ used in CAM3/CAM4 [in fact, CAM3/CAM4 computes a single-phase stratus fraction $a(\overline{u})$ with $\overline{u} = \alpha\overline{u}_l + (1 - \alpha)\overline{u}_i$, where α is a function of $\overline{T}$ and $\overline{u}_i = \overline{q}_v/q_{s,i}(\overline{T}, p)$].

CAM5 generates slightly smaller a_l than CAM3/CAM4. As $a_l \to 1$, CAM5 satisfies $\hat{u}_{l,\text{clr}} \to 1$ [$\hat{u}_{l,\text{clr}} \equiv (\overline{u}_l - a_l)/(1 - a_l)$ is mean RH over water averaged over the clear portion], consistent with what is likely to be observed in nature, but CAM3/CAM4 do not satisfy this condition since $\hat{u}_{l,\text{clr}} \to 0.5(1 + u_{cl})$ as $a_l \to 1$. By construction, our triangular PDF always satisfies $a_l \leq \overline{u}_l$ [Eq. (A8) and Fig. A1 (bottom)], so that $\hat{u}_{l,\text{clr}} \geq 0$. This allows the radiation scheme to separately handle $\tilde{q}_v$ (where the tilde denotes the average in the clear portion outside of the cloud) and $\hat{q}_{v,\text{cld}}$ in each grid layer, so that more realistic computations of radiative flux profiles and LW CRF will be possible in the future CAM (see section 3a).

In principle, triangular PDF can be used to diagnose $\hat{q}_l$ (or equivalently $\overline{Q}_l$) as well as a_l as shown in Eqs. (A3) and (A6). However, CAM5 continues to use the prognostic condensation scheme to compute $\overline{Q}_l$, as detailed in the next section. We plan to use the triangular PDF to consistently diagnose both a_l and $\overline{Q}_l$ with the PDF width $(\Delta v_l = \hat{u}_l - u_{cl})$ internally computed rather than specified, so that stratus macrophysics can be seamlessly applied across any horizontal and vertical resolution of a GCM grid.

b. Grid-mean net condensation rate of water vapor into liquid stratus condensate $\overline{Q}_l$

To compute $\overline{Q}_l$ (defined here as condensation rate minus evaporation rate), CAM5 follows the approach of Zhang et al. (2003) that was used in CAM3/CAM4, but with substantial refinements to the implementation and formulations, in order to be consistent with the reconstructed cloud structures in CAM5. We define saturation equilibrium as the state that satisfies the following two conditions: 1) RH over water within liquid stratus is always 1 ($\hat{u}_l = 1$) and 2) liquid stratus condensate does not exist outside of a_l. The sufficient and necessary constraints to compute $\overline{Q}_l$ in CAM5 are that, whenever any grid layer is perturbed from saturation equilibrium by various physics and dynamic processes, the system tries to restore saturation equilibrium.

Let us assume that one GCM grid layer is in saturation equilibrium at a certain moment. During the model time step Δt, the layer is perturbed by external forcings

(stratus microphysics, radiation, moist turbulence, grid-scale advection, deep and shallow convections, etc.). To restore saturation equilibrium, $\overline{Q}_l$ should be initiated within the layer. The changes of $\overline{q}_{l,\text{st}} = A_{l,\text{st}}\hat{q}_{l,\text{st}}$ during Δt [here, $A_{l,\text{st}} = (1 - A_{\text{cu}})a_{l,\text{st}}$ as in Eq. (5)] is the sum of $\overline{Q}_l$ and the grid-mean external forcings of liquid condensates $\overline{F}_l$,

$$\overline{Q}_l = \dot{\overline{q}}_{l,\text{st}} - \overline{F}_l = A_{l,\text{st}}\dot{\hat{q}}_{l,\text{st}} + c\hat{q}_{l,\text{st}}\dot{A}_{l,\text{st}} - \overline{F}_l, \quad \text{(A9)}$$

where $0 \leq c \leq 1$ is the ratio of $\hat{q}_{l,\text{st}}$ of newly formed or dissipated stratus to the preexisting $\hat{q}_{l,\text{st}}$. The $\dot{\phi}$ denotes time tendency of ϕ. If condensate within $A_{l,\text{st}}$ is internally homogeneous (heterogeneous), it will be $c = 1$ ($c < 1$). CAM5 uses $c = 0.1$, but the overall simulation is insensitive to c. Using the saturation equilibrium constraints, we can derive the following simultaneous linear equations:

$$a_{11}\dot{\hat{q}}_{l,\text{st}} + a_{12}\dot{A}_{l,\text{st}} = b_1 \quad \text{and}$$
$$a_{21}\dot{\hat{q}}_{l,\text{st}} + a_{22}\dot{A}_{l,\text{st}} = b_2, \quad \text{(A10)}$$

where individual coefficients a_{ij} and b_i are

$$a_{11} = \gamma A_{l,\text{st}}, \quad a_{12} = G + \gamma c\hat{q}_{l,\text{st}},$$

$$a_{21} = \alpha + \left(\frac{L_v}{C_p}\right)\hat{\beta}A_{l,\text{st}}, \quad a_{22} = \left(\frac{L_v}{C_p}\right)\hat{\beta}c\hat{q}_{l,\text{st}} \quad \text{and}$$

$$\text{(A11)}$$

$$b_1 = \alpha\dot{\overline{q}}_{t,\text{all}} - \beta\dot{\overline{T}}_{l,\text{all}} - Ga_{l,\text{st}}\dot{a}_{\text{cu}}, \quad b_2 = \alpha\dot{\hat{q}}_{t,\text{all}} - \beta\dot{\overline{T}}_{l,\text{all}},$$

with

$$\alpha = \left(\frac{1}{q_{s,w}}\right), \quad \beta = \left(\frac{\overline{q}_v}{q_{s,w}^2}\right)\left(\frac{\partial q_{s,w}}{\partial T}\right),$$

$$\hat{\beta} = \alpha\left(\frac{\partial q_{s,w}}{\partial T}\right), \quad \gamma = \alpha + \left(\frac{L_v}{C_p}\right)\beta \quad \text{and} \quad \text{(A12)}$$

$$G = \left(\frac{1}{1 - a_{\text{cu}}}\right)\left(\frac{\partial a_{l,\text{st}}}{\partial \overline{u}}\right)^{-1}$$

and

$$\dot{\overline{q}}_{t,\text{all}} = \dot{\overline{q}}_{v,\text{adv}} + \dot{\overline{q}}_{l,\text{adv}} + \dot{\overline{q}}_{v,\text{mic}} + \dot{\overline{q}}_{l,\text{mic}}, \quad \text{(A13)}$$

$$\dot{\overline{T}}_{l,\text{all}} = \dot{\overline{T}}_{\text{adv}} + \dot{\overline{T}}_{\text{mic}} - \left(\frac{L_v}{C_p}\right)(\dot{\overline{q}}_{l,\text{adv}} + \dot{\overline{q}}_{l,\text{mic}}),$$

$$\dot{\hat{q}}_{t,\text{all}} = \dot{\overline{q}}_{v,\text{adv}} + \dot{\overline{q}}_{l,\text{adv}} + \dot{\hat{q}}_{l,\text{mic}}, \quad \text{and}$$

$$\dot{\hat{q}}_{l,\text{mic}} = \frac{\dot{\overline{q}}_{l,\text{mic}}}{A_{\text{st}}},$$

where $\dot{\overline{\phi}}$ denotes grid-mean tendency and subscript all denotes all processes except for stratus macrophysics, which is the sum of stratus microphysics (subscript mic) and the other processes denoted by subscript adv (e.g., radiation, moist turbulence, grid-scale advection, and deep and shallow convections). In Eq. (A13), we use A_{st} instead of $A_{l,st}$ since stratus microphysics is formulated using a single-phase stratus fraction, $A_{st} = \max(A_{l,st}, A_{i,st})$. The above formulation was derived based on the assumption that 1) temperature is uniform within the grid, 2) stratus microphysics does not change water vapor within $a_{l,st}$, and 3) all forcings except stratus microphysics are uniformly applied into the grid. From Eqs. (3), (5), and (A9) and $\overline{F}_l = \overline{q}_{l,adv} + \overline{q}_{l,mic}$, we can compute $\overline{Q}_l$.

Although $A_{l,st}$ is explicitly used in computing $\overline{Q}_l$, the updated $\overline{q}_{l,st}(t + \Delta t)$ is not necessarily consistent with the updated $A_{l,st}(t + \Delta t)$. For example, it can be $\overline{q}_{l,st}(t + \Delta t) = 0$ but $A_{l,st}(t + \Delta t) > 0$ (so-called empty status) or $\overline{q}_{l,st}(t + \Delta t) > 0$ but $A_{l,st}(t + \Delta t) = 0$ (so-called infinitely dense stratus). This inconsistency between stratus fraction and in-stratus condensate is caused by the combined use of diagnostic stratus fraction and prognostic stratiform condensation schemes. To prevent this inconsistency, we additionally condense water vapor or evaporate stratus liquid droplets until $\hat{q}_{l,st}(t + \Delta t)$ falls within the externally specified ranges, $2 \times 10^{-4} \leq \hat{q}_{l,st}(t + \Delta t) \leq 3 \, \mathrm{g \, kg^{-1}}$. This pseudo condensation–evaporation adjustment conserves $\overline{q}_{l,st}(t + \Delta t)$ and always satisfies the diagnostic stratus fraction formula [Eq. (3)]. This adjustment is not performed if $\overline{q}_{l,st}(t + \Delta t) = 0$ and $A_{l,st}(t + \Delta t) = 0$ before the adjustment. In the case of ice stratus, rather than performing pseudo deposition–sublimation, CAM5 simply modifies $A_{i,st}(t + \Delta t)$ such that $\hat{q}_{i,st}(t + \Delta t)$ falls within the externally specified ranges, $2 \times 10^{-4} \leq \hat{q}_{i,st}(t + \Delta t) \leq 5 \, \mathrm{g \, kg^{-1}}$, which violates the diagnostic ice stratus fraction formula [Eq. (4)] after adjustment.

c. Imposing consistency between liquid stratus fraction and liquid stratus condensate

To reduce numerical instability due to the use of a long model integration time step ($\Delta t = 1200 \, \mathrm{s}$ for the Eulerian dynamic core or $1800 \, \mathrm{s}$ for the finite-volume dynamic core), CAM has used process splitting: that is, in each time step, successive parameterizations operate on the updated state resulting from the previous parameterization, as shown in Fig. 1. This process splitting allows for the use of separate shallow and deep convection schemes, because, in the case of time splitting (in which all parameterizations are operating on the same input state), a simultaneous use of two separate convection schemes can cause overstabilization of the

atmospheric column because of double counting of the convective adjustment. However, since multiple values of stratus fraction can be computed in each time step because of continuous updates of grid-mean RH after individual parameterization, process splitting raises a question on what is the best stratus fraction that all parameterizations should commonly use at each time step. During CAM5 development procedure, we found that CAM3 frequently generated unreasonably large $\hat{q}_{l,st}$. For example, in the ambiguous layer (i.e., the layer just above the PBL top) over the California stratocumulus deck, CAM3-simulated $a_{l,st}$ was only 0.2 but $\hat{q}_{l,st}$ was $4 \, \mathrm{g \, kg^{-1}}$, much larger than the maximally observable value of $1 \, \mathrm{g \, kg^{-1}}$ in nature. An offline test of CAM3 stratus macrophysics scheme revealed that this peculiar feature was associated with an inappropriate choice of input for $a_{l,st}$ in computing $\overline{Q}_l$.

To elucidate this problem, we pick the initial equilibrium state of $p = 900 \, \mathrm{hPa}$, $\overline{T} = 280 \, \mathrm{K}$, and $\overline{q}_t = 7 \, \mathrm{g \, kg^{-1}}$, representing a typical state of the ambiguous layer in the subtropical stratocumulus deck. According to the triangular PDF scheme that will be used as a benchmark framework mimicking nature, this initial equilibrium state corresponds to $\overline{q}_v = 6.84 \, \mathrm{g \, kg^{-1}}$, $\overline{q}_l = 0.16 \, \mathrm{g \, kg^{-1}}$, $a_{l,st} = 0.6$, and $\hat{q}_{l,st} = 0.26 \, \mathrm{g \, kg^{-1}}$ when $\Delta v = 0.1$ is chosen. A critical relative humidity of $u_{cl} = 0.943$ was selected in such a way that CAM3/CAM4's quadratic stratus fraction formula produces the same stratus fraction as the triangular PDF scheme at the initial equilibrium state. We forced the initial equilibrium state with a set of grid-mean external advective forcings of temperature and water vapor in a wide range ($-10 \leq \dot{\overline{T}}_{adv} \leq 10 \, \mathrm{K \, day^{-1}}$, $-10 \leq \dot{\overline{q}}_{v,adv} \leq 10 \, \mathrm{g \, kg^{-1} \, day^{-1}}$) and computed $\Delta a_{l,st}$ and $\Delta \hat{q}_{l,st}$ from the initial equilibrium state using both the prognostic condensation and full triangular PDF-based stratus macrophysics schemes [here, "full" means that not only $a_{l,st}$ but also $\hat{q}_{l,st}$ (or equivalently $\overline{Q}_l$) are computed together by the triangular PDF scheme]. We ran the following three configurations of prognostic stratus macrophysics scheme: (i) CAM3 configuration in which net condensation rate $\overline{Q}_l$ is computed using a non-equilibrium $a_{l,st}^{ne}$ obtained by applying external advective forcings ($\overline{T}_{adv}, \dot{\overline{q}}_{v,adv}$) to the initial equilibrium state and $a_{l,st}$ after stratus macrophysics is set to $a_{l,st}^{ne}$; (ii) CAM4 configuration, which is identical to CAM3 except that $a_{l,st}$ is updated at the end of the stratus macrophysics, using the prognosed grid-mean RH that includes all $\dot{\overline{T}}_{adv}, \dot{\overline{q}}_{v,adv}$ and $\overline{Q}_l$; and (iii) CAM5 configuration, in which $\overline{Q}_l$ is computed using the initial equilibrium state and $a_{l,st}$ is updated at the end of stratus macrophysics using the prognosed grid-mean RH. Simply speaking, $a_{l,st}$ in CAM3 (CAM5) is computed at the beginning (end) of stratus macrophysics while CAM4 computes $a_{l,st}$ both at the
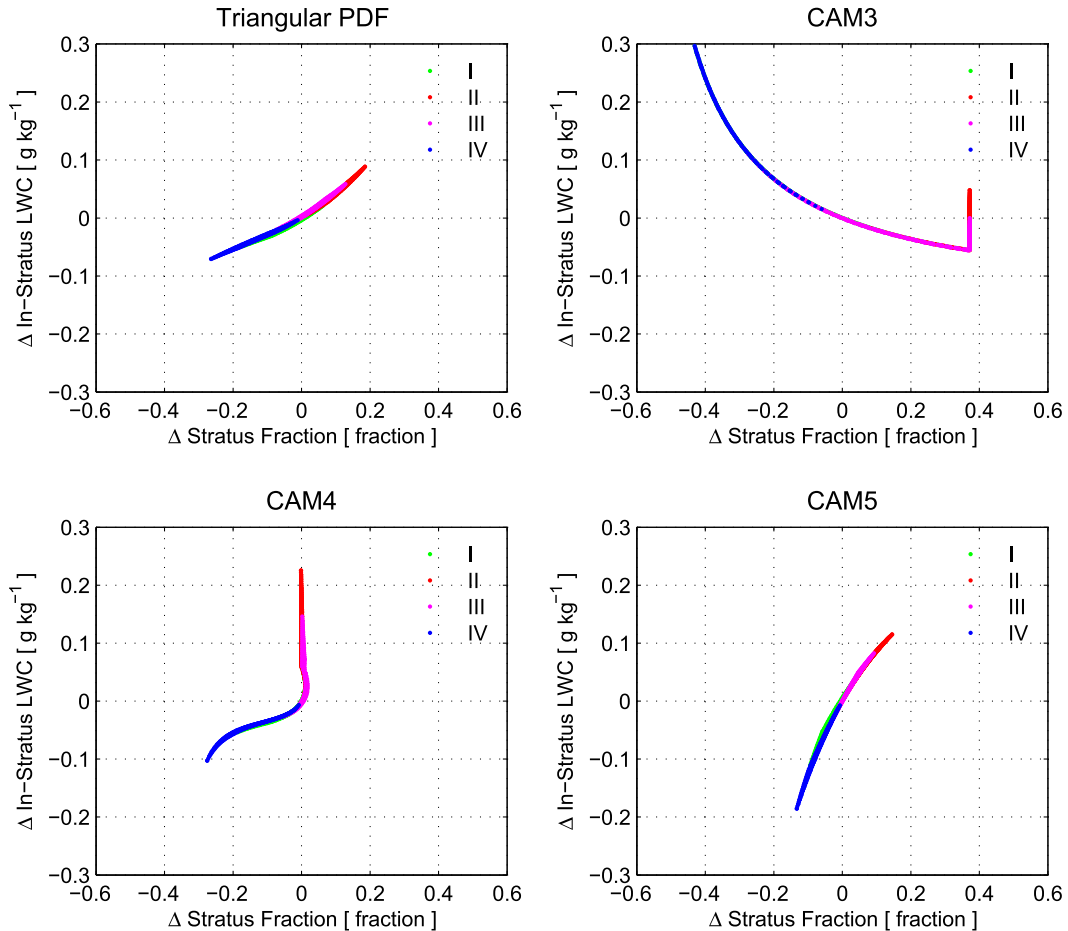
FIG. A2. Changes of liquid stratus fraction ($\Delta a_{l,\text{st}}$) and in-stratus LWC ($\Delta \hat{q}_{l,\text{st}}$) when advective forcings of temperature ($\overline{T}_{\text{adv}}$ K day^{-1}) and water vapor ($\overline{q}_{v,\text{adv}}$ g kg^{-1} day^{-1}) are applied to the initial saturation equilibrium state: green dots denote the cases of $\overline{T}_{\text{adv}} > 0$ and $\overline{q}_{v,\text{adv}} > 0$ (case I); red dots denote the cases of $\overline{T}_{\text{adv}} < 0$ and $\overline{q}_{v,\text{adv}} > 0$ (case II); magenta dots denote the cases of $\overline{T}_{\text{adv}} < 0$ and $\overline{q}_{v,\text{adv}} < 0$ (case III); and blue dots denote the cases of $\overline{T}_{\text{adv}} > 0$ and $\overline{q}_{v,\text{adv}} < 0$ (case IV). See text for detailed description on each of 4 cases (triangular PDF, CAM3, CAM4, and CAM5), including simulation settings.

beginning and end of stratus macrophysics. For simplicity, we neglected cumulus ($a_{\text{cu}} = 0$), precipitation ($\dot{\overline{q}}_{l,\text{mic}} = \dot{\hat{q}}_{l,\text{mic}} = \dot{\overline{q}}_{v,\text{mic}} = \dot{\overline{T}}_{\text{mic}} = 0$), and advection of condensate ($\dot{\overline{q}}_{l,\text{adv}} = 0$). In case of the triangular PDF scheme, condensation heating induced by external advective forcing was reassigned into the system with corresponding PDF adjustment until a convergent state was obtained.

Figure A2 shows the scatterplot of $\Delta a_{l,\text{st}}$ and $\Delta \hat{q}_{l,\text{st}}$ during $\Delta t = 1800$ s. Each dot corresponds to different values of $\dot{\overline{T}}_{\text{adv}}$ and $\dot{\overline{q}}_{v,\text{adv}}$. In case of the triangular PDF and CAM5 prognostic condensation schemes, $\hat{q}_{l,\text{st}}$ increases as $a_{l,\text{st}}$ increases. The behaviors of prognostic stratus macrophysics in CAM3 and CAM4 are problematic. In the warm and dry advection regimes (blue dots), CAM4 shows improved features over CAM3. In the cold and moist advection regimes (red dots), however, both CAM3 and CAM4 show little changes to $a_{l,\text{st}}$,

though $\hat{q}_{l,\text{st}}$ rapidly increases, which explains why CAM3 produces small $a_{l,\text{st}}$ but very large $\hat{q}_{l,\text{st}}$. This undesirable inconsistency between $a_{l,\text{st}}$ and $\hat{q}_{l,\text{st}}$ in CAM3/CAM4 stems from the use of inappropriate $a_{l,\text{st}}$ as an input to the prognostic condensation scheme. Since the prognostic condensation scheme is an adjustment process from one saturation equilibrium state to another saturation equilibrium state, $\overline{Q}_l$ should be computed using $a_{l,\text{st}}$ at the equilibrium state (as in CAM5), not at the nonequilibrium state (as in CAM3/CAM4).

APPENDIX B

Description of the Various Simulations

This section provides a brief description of the configurations of various CAM5 simulations. The basic

settings common to all simulations, detailed below, are as follows:

- model physics time step of $\Delta t = 1800$ s, radiation time step of $\Delta t = 3600$ s, and dynamic sub–time step of $\Delta t = 225$ s;
- horizontal resolution of 1.9° latitude $\times$ 2.5° longitude; and
- 30 vertical layers with the midpoint height of the lowest model layer $[z(1)]$ at the sigma pressure level of $\sigma = 0.9926$, corresponding to ~ 67 m over the ocean, and the highest model interface at $\sigma = 0.00225$.

Below 800 hPa, CAM5 has 4 more layers than CAM4 (which has 26 layers in total) but $z(1)$ of CAM4 is identical to the $z(1)$ of CAM5.

a. Stand-alone CAM5 simulation forced by climatological SST in the year 2000

This simulation is forced by observed climatological SST and sea ice fraction with annual cycle (Hurrell et al. 2008). One-dimensional ice thermodynamics (i.e., vertical exchanges of heat and moisture) is active assuming sea ice thickness is 2 (1) m over the Arctic (Antarctic) and ocean temperature below sea ice is fixed at -1.8°C. Snow fraction over ice is a function of snow depth, which is controlled by snowfall rate from the atmosphere. Snow albedo, which is generally larger than the sea ice albedo at the clean state, can decrease when atmospheric aerosols (e.g., black carbon) are deposited onto the snow. The land model is fully interactive with the atmosphere. The atmospheric concentration of individual greenhouse gases is specified as a fixed value over the entire atmosphere without annual cycle ($CO_2 = 367$, $CH_4 = 1760 \times 10^{-3}$, $N_2O = 316 \times 10^{-3}$, CFC-11 $= 653.45 \times 10^{-6}$, and CFC-12 $= 535 \times 10^{-6}$; all in units of ppmv). Atmospheric concentration of ozone is also specified as a function of (x, y, z) with a specified annual cycle. Solar constant is specified as a fixed value without annual cycle. Surface fluxes of various aerosol species are also specified in the year 2000. No major volcanic aerosols are added in this simulation.

b. CAM5–AMIP

This simulation is identical to the above stand-alone CAM5 simulation, except that

- all of the specified SST, sea ice fraction, greenhouse gases, ozone, solar constant, and surface flux of aerosols have interannual variations derived from the observations and
- atmospheric concentrations of the major volcanic aerosols are specified as a function of (y, z, t) with annual cycle with specified effective radii.

c. CAM5–SOM

This is a CAM5 simulation coupled with an SOM with adjusive surface fluxes of heat and moisture designed to mimic the effects of oceanic horizontal advection in the fully coupled CESM1 simulation. A long-term CAM5–SOM is run (with the configurations of the above stand-alone CAM5 but in the year 1850 with constant $CO_2 = 284.7$, $CH_4 = 791.6 \times 10^{-3}$, $N_2O = 275.68 \times 10^{-3}$, CFC-11 $= 12.48 \times 10^{-6}$, and CFC-11 $= 0$; all in units of ppmv) without the specifications of SST and sea ice fraction, until it reaches the stable equilibrium state.

d. CESM1

This is a fully coupled simulation without any flux correction between atmosphere and underlying surfaces. The specifications of greenhouse gases, ozone, solar constant, surface fluxes of aerosols, and major volcanic aerosols are identical to the CAM5–AMIP, except that full interannual variations from 1850 to 2005 are included.

REFERENCES

Bennartz, R., 2007: Global assessment of marine boundary layer cloud droplet number concentration from satellite. *J. Geophys. Res.,* **112,** D02201, doi:10.1029/2006JD007547.

Bodas-Salcedo, A., K. Williams, P. Field, and A. Lock, 2012: The surface downwelling solar radiation surplus over the Southern Ocean in the Met Office model: The role of midlatitude cyclone clouds. *J. Climate,* **25,** 7467–7486, doi:10.1175/JCLI-D-11-00702.1.

Bretherton, C., and S. Park, 2009: A new moist turbulence parameterization in the Community Atmosphere Model. *J. Climate,* **22,** 3422–3448, doi:10.1175/2008JCLI2556.1.

Hack, J., 1994: Parameterization of moist convection in the National Center for Atmospheric Research Community Climate Model (CCM2). *J. Geophys. Res.,* **99,** 5551–5568, doi:10.1029/93JD03478.

Hahn, C. J., and S. G. Warren, 1999: Extended edited synoptic cloud reports from ships and land stations over the globe, 1952–1996. U.S. Department of Energy Office of Biological and Environmental Research Environmental Sciences Division Publ. 4913, 88 pp.

Harrison, E., P. Minnis, B. Barkstrom, V. Ramanathan, R. Cess, and G. Gibson, 1990: Seasonal variation of cloud radiative forcing derived from the Earth Radiation Budget Experiment. *J. Geophys. Res.,* **95,** 18 687–18 703, doi:10.1029/JD095iD11p18687.

Holtslag, A., and B. Boville, 1993: Local versus nonlocal boundary-layer diffusion in a global climate model. *J. Climate,* **6,** 1825–1842, doi:10.1175/1520-0442(1993)006<1825:LVNBLD>2.0.CO;2.

Huffman, G. J., R. F. Adler, D. T. Bolvin, and G. Gu, 2009: Improving the global precipitation record: GPCP version 2.1. *Geophys. Res. Lett.,* **36,** L17808, doi:10.1029/2009GL040000.

Hurrell, J., J. Hack, D. Shea, J. Caron, and J. Rosinski, 2008: A new sea surface temperature and sea ice boundary dataset for the Community Atmosphere Model. *J. Climate,* **21,** 5145–5153, doi:10.1175/2008JCLI2292.1.

Iacono, M. J., J. Delamere, E. Mlawer, M. Shephard, S. Clough, and W. Collins, 2008: Radiative forcing by long-lived greenhouse gases: Calculations with the AER radiative transfer models. *J. Geophys. Res.,* **113,** D13103, doi:10.1029/2008JD009944.

Kalnay, E., and Coauthors, 1996: The NCEP/NCAR 40-Year Reanalysis Project. *Bull. Amer. Meteor. Soc.,* **77,** 437–471, doi:10.1175/1520-0477(1996)077<0437:TNYRP>2.0.CO;2.

King, D. M., S. Platnick, S. A. Ackerman, and P. A. Hubanks, 2013: Spatial and temporal distribution of clouds observed by MODIS onboard the *Terra* and *Aqua* satellites. *IEEE Geosci. Remote Sens.,* **51,** 3826–3852, doi:10.1109/TGRS.2012.2227333.

Klein, S. A., and D. L. Hartmann, 1993: The seasonal cycle of low stratiform clouds. *J. Climate,* **6,** 1587–1606, doi:10.1175/1520-0442(1993)006<1587:TSCOLS>2.0.CO;2.

Liu, X., and Coauthors, 2012: Toward a minimal representation of aerosols in climate models: Description and evaluation in the Community Atmosphere Model CAM5. *Geosci. Model Dev.,* **5,** 709–739, doi:10.5194/gmd-5-709-2012.

Loeb, N., B. Wielicki, D. Doelling, G. Smith, D. Keyes, S. Kato, N. Manalo-Smith, and T. Wong, 2009: Toward optimal closure of the earth's top-of-atmosphere radiation budget. *J. Climate,* **22,** 748–766, doi:10.1175/2008JCLI2637.1.

Morrison, H., and A. Gettelman, 2008: A new two-moment bulk stratiform cloud microphysics scheme in the Community Atmosphere Model, version 3 (CAM3). Part I: Description and numerical tests. *J. Climate,* **21,** 3642–3659, doi:10.1175/2008JCLI2105.1.

Neale, R., J. Richter, and M. Jochum, 2008: The impact of convection on ENSO: From a delayed oscillator to a series of events. *J. Climate,* **21,** 5904–5924, doi:10.1175/2008JCLI2244.1.

Park, S., 2014a: A unified convection scheme, UNICON. Part I. Formulation. *J. Atmos. Sci.,* in press.

——, 2014b: A unified convection scheme, UNICON. Part II. Simulation. *J. Atmos. Sci.,* in press.

——, and C. Leovy, 2004: Marine low-cloud anomalies associated with enso. *J. Climate,* **17,** 3448–3469, doi:10.1175/1520-0442(2004)017<3448:MLAAWE>2.0.CO;2.

——, and C. Bretherton, 2009: The University of Washington shallow convection and moist turbulence schemes and their impact on climate simulations with the Community Atmosphere Model. *J. Climate,* **22,** 3449–3469, doi:10.1175/2008JCLI2557.1.

——, C. Deser, and M. Alexander, 2005: Estimation of the surface heat flux response to sea surface temperature anomalies over the global oceans. *J. Climate,* **18,** 4582–4599, doi:10.1175/JCLI3521.1.

——, M. Alexander, and C. Deser, 2006: The impact of cloud radiative feedback, remote ENSO forcing, and entrainment on the persistence of North Pacific sea surface temperature anomalies. *J. Climate,* **19,** 6243–6261, doi:10.1175/JCLI3957.1.

Prabha, T. V., A. Khain, R. Maheshkumar, G. Pandithurai, J. Kulkarni, M. Konwar, and B. Goswami, 2011: Microphysics of premonsoon and monsoon clouds as seen from in situ measurements during the Cloud Aerosol Interaction and Precipitation Enhancement Experiment (CAIPEEX). *J. Atmos. Sci.,* **68,** 1882–1901, doi:10.1175/2011JAS3707.1.

Ramanathan, V., R. Cess, E. Harrison, P. Minnis, B. Barkstrom, E. Ahmad, and D. Hartmann, 1989: Cloud-radiative forcing and climate: Results from the Earth Radiation Budget Experiment. *Science,* **243,** 57–63, doi:10.1126/science.243.4887.57.

Randel, D. L., T. J. Greenwald, T. H. Vonder Haar, G. L. Stephens, M. A. Ringerud, and C. L. Combs, 1996: A new global water vapor dataset. *Bull. Amer. Meteor. Soc.,* **77,** 1233–1246, doi:10.1175/1520-0477(1996)077<1233:ANGWVD>2.0.CO;2.

Rasch, P., and J. Kristjansson, 1998: A comparison of the CCM3 model climate using diagnosed and predicted condensate parameterization. *J. Climate,* **11,** 1587–1614, doi:10.1175/1520-0442(1998)011<1587:ACOTCM>2.0.CO;2.

Richter, J., and P. Rasch, 2008: Effects of convective momentum transport on the atmospheric circulation in the Community Atmosphere Model, version 3. *J. Climate,* **21,** 1487–1499, doi:10.1175/2007JCLI1789.1.

Rossow, W., and R. Schiffer, 1991: ISCCP cloud data products. *Bull. Amer. Meteor. Soc.,* **72,** 2–20, doi:10.1175/1520-0477(1991)072<0002:ICDP>2.0.CO;2.

Smith, R., 1990: A scheme for predicting layer clouds and their water content in a general circulation model. *Quart. J. Roy. Meteor. Soc.,* **116,** 435–460, doi:10.1002/qj.49711649210.

Stephens, G. L., and Coauthors, 2012: An update on Earth's energy balance in light of the latest global observations. *Nat. Geosci.,* **5,** 691–696, doi:10.1038/ngeo1580.

Williams, K., and Coauthors, 2013: The Transpose-AMIP II experiment and its application to the understanding of Southern Ocean cloud biases in climate models. *J. Climate,* **26,** 3258–3274, doi:10.1175/JCLI-D-12-00429.1.

WMO, 1975: Manual on the observation of clouds and other meteors: Volume I. WMO Publication 407, 155 pp.

Xie, P., and P. Arkin, 1996: Analyses of global monthly precipitation using gauge observations, satellite estimates, and numerical model predictions. *J. Climate,* **9,** 840–858, doi:10.1175/1520-0442(1996)009<0840:AOGMPU>2.0.CO;2.

Zhang, M., W. Lin, C. Bretherton, J. Hack, and P. Rasch, 2003: A modified formulation of fractional stratiform condensation rate in the NCAR Community Atmospheric Model (CAM2). *J. Geophys. Res.,* **108,** 4035, doi:10.1029/2002JD002523.

Zhang, Y., W. Rossow, A. Lacis, V. Oinas, and M. Mishchenko, 2004: Calculation of radiative fluxes from the surface to top of atmosphere based on ISCCP and other global data sets: Refinements of the radiative transfer model and the input data. *J. Geophys. Res.,* **109,** D19105, doi:10.1029/2003JD004457.